2017

Locomotion At Low Reynolds Number: Dynamics In Newtonian And Non-Newtonian Systems With Biomedical Applications

David A. Gagnon
University of Pennsylvania, dgagnon@seas.upenn.edu

Locomotion At Low Reynolds Number: Dynamics In Newtonian And Non-Newtonian Systems With Biomedical Applications

Abstract
Swimming microorganisms such as bacteria, spermatozoa, algae, and nematodes are critical to ubiquitous biological phenomena such as disease and infection, ecosystem dynamics, and mammalian fertilization. While there has been much scientific and practical interest in studying these swimmers in Newtonian (water-like) fluids, there are fewer systematic experimental studies on swimming through non-Newtonian (non-water-like) fluids with biologically-relevant mechanical properties. These organisms commonly swim through viscoelastic, structured, or shear-rate-dependent fluids, such as blood, mucus, and living tissues. Furthermore, the small length scales of these organisms dictate that their motion is dominated by viscous forces and inertia is negligible. Using rheology, microscopy, particle tracking, and image processing techniques, we examine the interaction of low Reynolds number swimmers and non-Newtonian fluids including viscoelastic, locally-anisotropic, and shear-thinning fluids. We then apply our understanding of locomotion to the study of the genetic disease Spinal Muscular Atrophy.

Degree Type
Dissertation

Degree Name
Doctor of Philosophy (PhD)

Graduate Group
Mechanical Engineering & Applied Mechanics

First Advisor
Paulo E. Arratia

Keywords
Complex fluids, Fluid rheology, Swimming at low Reynolds number

Subject Categories
Physics

LOCOMOTION AT LOW REYNOLDS NUMBER: DYNAMICS IN NEWTONIAN AND NON-NEWTONIAN SYSTEMS WITH BIOMEDICAL APPLICATIONS

David A. Gagnon

A DISSERTATION

in

Mechanical Engineering and Applied Mechanics

Presented to the Faculties of the University of Pennsylvania

in

Partial Fulfillment of the Requirements for the

Degree of Doctor of Philosophy

2017

Supervisor of Dissertation

_____

Paulo E. Arratia, Professor and Associate Chair for Undergraduate Affairs
Mechanical Engineering and Applied Mechanics, University of Pennsylvania

Graduate Group Chairperson

_____

Kevin T. Turner, Professor, Associate Chair for Graduate Affairs, and Graduate Group Chair
Mechanical Engineering and Applied Mechanics, University of Pennsylvania

Dissertation Committee

Haim H. Bau, Professor
Mechanical Engineering and Applied Mechanics, University of Pennsylvania

Robert G. Kalb, MD, Professor of Neurology, University of Pennsylvania
Attending Neurologist, Philadelphia VA Medical Center
Attending Neurology, Hospital of the University of Pennsylvania

LOCOMOTION AT LOW REYNOLDS NUMBER: DYNAMICS IN NEWTONIAN AND NON-NEWTONIAN SYSTEMS WITH BIOMEDICAL APPLICATIONS

Dedicated to Lucy

ACKNOWLEDGEMENTS

My family for their love and support during the journey of my education.

Dorothy Cheney and Robert Seyfarth for providing a retreat from Philadelphia and sharing their wealth of knowledge about being a student, researcher, and teacher.

Eliot, Nicholas, and Hannah for bringing cheer when experiments fail and the third reviewer hates your paper.

Lucy Seyfarth for her unconditional help in my pursuit for data; for being my best friend and most ardent champion.

Matthews Turpin and Piccoli for providing comic relief; for being shining examples of leadership and scholarship during our studies at Penn; for always being ready ears, a steady allies, and a cunning opponents.

Kenny Breuer for fostering my love of fundamental research. He may not remember my first day in his lab as a freshman at Brown, but I certainly do; he gave me a very expensive Photron Fastcam and said, "Don't break it."

Jeff Guasto for introducing me to Paulo and providing guidance throughout my career.

Paulo Arratia for always taking science but not always the scientist seriously; for his uncanny ability to spot a poorly written draft from the first paragraph of the introduction; for humoring my sometimes quixotic scientific stories; for pushing when I was stuck, believing when I doubted myself, and extending a hand when I needed help; for being a teacher, mentor, colleague, and friend.

ABSTRACT

LOCOMOTION AT LOW REYNOLDS NUMBER: DYNAMICS IN NEWTONIAN AND NON-NEWTONIAN SYSTEMS WITH BIOMEDICAL APPLICATIONS

David A. Gagnon

Paulo E. Arratia

Swimming microorganisms such as bacteria, spermatozoa, algae, and nematodes are critical to ubiquitous biological phenomena such as disease and infection, ecosystem dynamics, and mammalian fertilization. While there has been much scientific and practical interest in studying these swimmers in Newtonian fluids, there are fewer systematic experimental studies on swimming through non-Newtonian fluids with biologically-relevant mechanical properties. These organisms commonly swim through viscoelastic, structured, or shear-rate-dependent fluids, such as blood, mucus, and living tissues. Furthermore, the small length scales of these organisms dictate that their motion is dominated by viscous forces and inertia is negligible. Using rheology, microscopy, particle tracking, and image processing techniques, we examine the interaction of low Reynolds number swimmers and non-Newtonian fluids including viscoelastic, locally-anisotropic, and shear-thinning fluids. We then apply our understanding of locomotion to the study of the genetic disease Spinal Muscular Atrophy.

TABLE OF CONTENTS

LIST OF ILLUSTRATIONS

CHAPTER 1 : Introduction

Swimming microorganisms are integral to many natural processes, including the formation of infectious biofilms in the stomach (Celli et al., 2009), the movement of sperm cells in cervical fluid (Katz and Berger, 1980; Fauci and Dillon, 2006), suspension feeding in oceans and lakes (Leptos et al., 2009), and the stabilization of soil ecosystems by nematodes (Alexander, 1991). Typical length scales for these organisms range from the micron (e.g. *Escherichia coli*) to the millimeter scale (e.g. *Caenorhabditis elegans*). The physics that governs swimming at these small length scales is fundamentally different from our typical interaction between a (human) swimmer and a fluid (Elfring et al., 2015). As a result, we begin by discussing the fundamental swimming problem: how does a organism move through a fluid when it is very small?

1.1. The swimming problem

At its most fundamental level, a microorganism swims by deforming its body, and by extension, deforming the solid-liquid interface at its surface (Elfring et al., 2015). Their typical locomotion strategies fall into one of three categories of swimming gait: *(i)* "pushers," which use rotating flagella (*E. coli*, Patteson et al. (2015)) or an undulatory filament (*C. elegans*, Korta et al. (2007); Sznitman et al. (2010b) and spermatozoa, Gray and Hancock (1955); Montenegro-Johnson et al. (2012)) to produce time-periodic body shapes like a corkscrew or traveling wave, respectively; *(ii)* "pullers," which swim by waving cilia in a time-periodic breast stroke pattern (*Chlamydomonas reinhardtii*, Qin et al. (2015); Leptos et al. (2009)); and *(iii)* "squirmers", which moves by generating metachronal waves via beating cilia covering their cell bodies (*Volvox*, Pedley et al. (2016)). These deformations, regardless of swimming gait, result in surface stresses and fluid motion and are a combination of rotation and translation.

We begin by considering the equation of motion for an arbitrary fluid element in the pres-

ence of a swimmer. For any given volume element, the rate of momentum accumulation must be equal to the net momentum flux across the surfaces plus the sum of pressure and volumetric forces (such as gravity) acting on the system. The momentum equation is:

$$\rho\left(\frac{\partial \boldsymbol{u}}{\partial t}+\boldsymbol{u}\cdot\boldsymbol{\nabla}\boldsymbol{u}\right)=-\boldsymbol{\nabla}p+\boldsymbol{\nabla}\cdot\boldsymbol{\tau}+\rho\boldsymbol{g}, \tag{1.1}$$

where each term from left to right represents fluid acceleration (rate of momentum increase plus convective acceleration), pressure forces, viscous forces, and body (volumetric) forces; here, ρ is the fluid density, $\boldsymbol{u}$ is the fluid velocity, p is pressure, $\boldsymbol{\tau}$ is the shear stress tensor, and $\boldsymbol{g}$ is gravitation acceleration. For the purposes of this discussion, we can also assume that the fluid is Newtonian and has constant viscosity μ. We can then write the constitutive equation only valid for incompressible and Newtonian fluids:

$$\boldsymbol{\tau}=\mu\dot{\boldsymbol{\gamma}}, \tag{1.2}$$

where the shear rate tensor $\dot{\boldsymbol{\gamma}}\equiv\frac{1}{2}\left(\boldsymbol{\nabla}\boldsymbol{u}+\boldsymbol{\nabla}\boldsymbol{u}^{\mathsf{T}}\right)$. Furthermore, we can simplify the fluid acceleration terms via the material derivative $\frac{D\boldsymbol{u}}{Dt}=\frac{\partial \boldsymbol{u}}{\partial t}+\boldsymbol{u}\cdot(\boldsymbol{\nabla}\boldsymbol{u})$. We can then write the more general momentum equation as the Navier-Stokes equation:

$$\rho\frac{D\boldsymbol{u}}{Dt}=-\boldsymbol{\nabla}p+\mu\boldsymbol{\nabla}^2\boldsymbol{u}+\rho\boldsymbol{g} \tag{1.3}$$

Equation (1.3) can be non-dimensionalized using the following scalings:

$$\boldsymbol{u}^* = \frac{\boldsymbol{u}}{U} \tag{1.4a}$$

$$p^* = \frac{P}{\mu U^2} \tag{1.4b}$$

$$t^* = \frac{tU}{L} \tag{1.4c}$$

$$r^* = \frac{r}{L} \tag{1.4d}$$

$$\boldsymbol{\nabla}^* = L\boldsymbol{\nabla} \tag{1.4e}$$

$$\frac{D}{Dt^*} = \left(\frac{L}{U}\right)\frac{D}{Dt}, \tag{1.4f}$$

where L, U, P, r and t are characteristic length, speed, pressure, position, and time, respectively. Substituting into Eq. (1.3) leads to the following non-dimensional equation of motion for an incompressible, Newtonian fluid:

$$\frac{D\boldsymbol{u}^*}{Dt^*} = -\boldsymbol{\nabla}^* p^* + \left[\frac{\mu}{LU\rho}\right]\boldsymbol{\nabla}^{*2}\boldsymbol{u}^* + \left[\frac{gL}{U^2}\right]\frac{\boldsymbol{g}}{g}. \tag{1.5}$$

The two non-dimensional groups in brackets are the Reynolds number $Re = \frac{\rho UL}{\mu}$ and the Froude number $Fr = \frac{U^2}{gL}$, where U is the swimming speed, L is a characteristic length scale, and ρ and η are the fluid's density and viscosity, respectively. Rewriting the equation with these numbers:

$$\frac{D\boldsymbol{u}^*}{Dt^*} = -\boldsymbol{\nabla}^* p^* + \left[\frac{1}{Re}\right]\boldsymbol{\nabla}^{*2}\boldsymbol{u}^* + \left[\frac{1}{Fr}\right]\frac{\boldsymbol{g}}{g}, \tag{1.6}$$

we can immediately see the impact of the small size of microorganisms L; these small length scales naturally lead to small Reynolds numbers and large Froude numbers. This means that body and inertial forces are negligible and viscous forces dominate the equation of motion. Intuitively, this makes sense, since volumetric forces scale as L^3 while surface or traction forces scale as L^2; additionally, the low Reynolds number regime for swimmers dictates that organisms use viscous drag forces to propel themselves through a fluid.

Simplifying Eq. 1.6 based on these assumptions, we obtain Stokes' equation for motion at low Reynolds number:

$$\boldsymbol{\nabla} p = \mu \boldsymbol{\nabla}^2 \boldsymbol{u}. \tag{1.7}$$

We also invoke conservation of mass and define continuity for an incompressible, constant density fluid:

$$\boldsymbol{\nabla} \cdot \boldsymbol{u} = 0. \tag{1.8}$$

In the low Reynolds number regime governed by these two equations, viscous forces dominate inertial forces, and fluid transport is independent of time or kinematically reversible. Consequently, an organism's body geometry dictates the motion of a low-*Re* swimmer; such an organism must employ a kinematically-irreversible swimming stroke for net translation to occur (Purcell, 1977).

If our fluid is not of constant viscosity, we can write a more general equation of motion which does not presuppose the constitutive equation of the fluid. Defining the total stress tensor $\boldsymbol{\sigma} = -p\boldsymbol{I} + \boldsymbol{\tau}$, we can write Stokes' equation as:

$$\boldsymbol{\nabla} p = \boldsymbol{\nabla} \cdot \boldsymbol{\tau} \tag{1.9}$$

or equivalently

$$\boldsymbol{\nabla} \cdot \boldsymbol{\sigma} = 0. \tag{1.10}$$

Since a microorganism is freely swimming with no external forces or torques acting upon its body, it is instantaneously force- and torque-free. This indicates that for any given swimmer geometry or body shape $S(t)$, the force F and torque L on the swimmer's body are expressed as:

$$F = \int_S \boldsymbol{n} \cdot \boldsymbol{\sigma} \mathrm{d}S = 0 \tag{1.11}$$

$$L = \int_S \boldsymbol{r} \times (\boldsymbol{n} \cdot \boldsymbol{\sigma}) \, \mathrm{d}S = 0, \tag{1.12}$$

where $\boldsymbol{r}$ is the position vector from the swimmer's centroid to the surface $S(t)$. Note that these forces and torques are only dependent on body shape of the swimmer and fluid stresses from the aforementioned fundamental equations (1.8) and (1.10) and sum to zero (Elfring et al., 2015).

We can then extend these equations to estimate the mechanical power or cost of swimming for a low Reynolds number swimmer, which will be discussed in more detail in Section 3.5; this framework is also the foundation for simple analytical models of self-propulsion (Taylor, 1951; Gray and Hancock, 1955; Lighthill, 1976).

While many studies have sought an understanding of self-propulsion at low *Re* in Newtonian fluids (Taylor, 1951; Lighthill, 1976; Korta et al., 2007; Lauga and Powers, 2009; Guasto et al., 2010; Padmanabhan et al., 2012; Bilbao et al., 2013), there are crucial biological systems in which microorganisms must swim in complex fluids that contain polymers, particles, and large proteins (Spagnolie, 2015). Examples include sperm cells in cervical mucus (Katz and Berger, 1980; Fauci and Dillon, 2006) and Lyme disease spirochetes in tissues (Harman et al., 2012). These complex fluids typically display non-Newtonian rheological behavior such as shear-thinning viscosity and viscoelasticity (Larson, 1999). Furthermore, many biologically-relevant systems present geometries that combine a swimmer's interaction with complex fluids with confinement, which can further modify the stresses on (and behavior of) the organism.

Recent studies of the behavior of single swimmers in non-Newtonian fluids have centered on the effects of fluid elasticity and local structure on propulsion speed and kinematics (Lauga, 2007; Fu et al., 2009; Leshansky, 2009; Fu et al., 2010; Teran et al., 2010; Juarez et al., 2010; Shen and Arratia, 2011; Liu et al., 2011; Harman et al., 2012; Gagnon et al., 2013, 2014b; Thomases and Guy, 2014a; Patteson et al., 2015; Qin et al., 2015). These studies have shown that fluid elasticity modifies the swimming speed and kinematics of microorganisms. Whether swimming speed is increased or decreased seems highly dependent on the

swimming gait of the organism and its coupling with the material properties of the fluid. With this perspective, there are three broad aims within the scope of this work:

1.2. Perform systematic studies of swimming in fluids with non-Newtonian viscosity behavior

To date, major studies of the effects of shear-thinning viscosity have been theoretical (Vélez-Cordero and Lauga, 2013) and numerical (Montenegro-Johnson et al., 2012, 2013). The theoretical analysis focused on a two-dimensional, infinite waving sheet immersed in a model Carreau (shear-thinning) fluid, and found a non-Newtonian contribution to propulsion speed to fourth order in amplitude when the sheet was extensible, but no non-Newtonian contribution to propulsion speed when an inextensible condition was applied (Vélez-Cordero and Lauga, 2013). Additionally, for a finite swimmer, this analysis suggested the flow field was modified, with increased vorticity near the sheet (Vélez-Cordero and Lauga, 2013). Separate simulations (Montenegro-Johnson et al., 2012, 2013) also using the Carreau model suggested that undulatory swimmers with a head or "payload" (similar to a sperm cell) are assisted by shear-thinning viscosity, resulting in increased speed and that the swimmer's motion results in an envelope of thinned fluid around the body.

Despite these recent and important efforts, there is still a dearth of experimental investigations of swimming in shear-thinning fluids, and the effects of rate-dependent viscosity on swimming remain unclear. Experiments with a mechanical model system (Dasgupta et al., 2013) finds a decrease in propulsion for fluids possessing both shear-thinning and viscoelastic behavior, while the swimming speed of *C. elegans* is shown to be unaffected by shear-thinning viscosity (Shen and Arratia, 2011) although only a single data point is available. One particularly important outstanding question is whether a microorganism finds swimming in shear-thinning fluids mechanically easier (or more difficult) than in Newtonian fluids. One can think of this ease or difficulty in swimming as an organism's cost of swimming, or mechanical power. Recent work, both theoretical (Vélez-Cordero

and Lauga, 2013) and numerical (Li and Ardekani, 2015), has also proposed a reduction in the cost of swimming for undulatory organisms in shear-thinning fluids. Indeed, it seems quite reasonable that a fluid possessing decreasing viscosity with increasing shear rate might reduce the cost of swimming, although there has been little experimental evidence for such behavior.

1.3. Examine swimming under anisotropic conditions, including confinement in non-Newtonian fluids

Of additional interest is the ability of microoganisms to swim under confinement. By introducing a far-field no-slip boundary condition, one can mimic natural biological processes such as bacteria moving through vesicles in the circulatory system and sperm cells swimming through millimeter-scale fallopian tubes (Colburn, 1986); both of these systems contain non-Newtonian fluids (blood and mucus, respectively). Building off our above argument that non-Newtonian fluids are the most appropriate model system for studying biological locomotion, we believe a necessary component of studying low Reynolds number swimmers is a systematic experimental investigation of swimming under confinement in non-Newtonian fluids.

An analytical study (Katz, 2003) and a numerical computation (Münch et al., 2016) using an infinite waving sheet in the presence of solid boundaries have proposed that an undulatory swimmer should swim faster under confinement in a Newtonian fluid. Several studies have shown that hydrodynamic wall interactions can also lead to aggregation in Newtonian fluids (Li and Ardekani, 2014), and modified aggregation in viscoelastic fluids (Yazdi et al., 2014, 2015). Additionally, work with *C. elegans* has shown that the presence of solid boundaries can lead a modulated swimming gait, particularly a decrease in amplitude in Newtonian fluids (Schulman et al., 2014). However, there is a lack of experimental data on the combined effects of viscoelasticity and confinement on swimming behavior. We therefore combine effects of confinement and fluids with viscoelastic and shear-thinning

rheology and examine their fundamental effects on the kinematics of an undulatory swimmer. For *C. elegans* swimming through a thin channel, as the walls of the channel approach the characteristic transverse length-scale of the nematode's swimming gate, defined as the head amplitude, we expect modifications of the flow field around the swimmer, which in turn will modify fluid stresses and simultaneously the nematode's swimming behavior.

1.4. Apply swimming assays to the study of genetic disease

Previously, a similar assay has described a number of genotypes of *C. elegans*, including one with the genetic disease muscular dystrophy (Krajacic et al., 2012; Sznitman et al., 2010a). In this study, we use a swimming assay incorporating both kinematics (e.g. swimming speed) and dynamics (e.g. bending force) to examine the swimming behavior of four groups of *C. elegans*: control groups N2 (wildtype) and the long-lived mutant *daf-2(e1370)*, a diseased group *smn-1(ok355)*, and a rescue group *smn-1(ok355);daf-2(e1370)*. By observing this periodic motion during forward swimming, we are able to detect statistically significant differences between the diseased and rescue groups for two important factors: bending force and mechanical power. Bending force indicates the forces required to bend the nematode's body into the observed configurations and mechanical power represents the rate of energy expenditure for the nematode's forward progress.

1.4.1. Methods

1.5. *C. elegans*: a model biological organism

Swimming experiments in Newtonian and non-Newtonian fluids are performed using the nematode *C. elegans*. These nematodes are characterized by a relatively long and quasi-cylindrical body shape and are approximately 1 mm in length and 80 µm in diameter; their genome has been completely sequenced (Brenner, 1974) and a complete cell lineage has been established (Byerly et al., 1976). *C. elegans* are equipped with 95 muscle cells that are highly similar in both anatomy and molecular makeup to vertebrate skeletal muscle (White

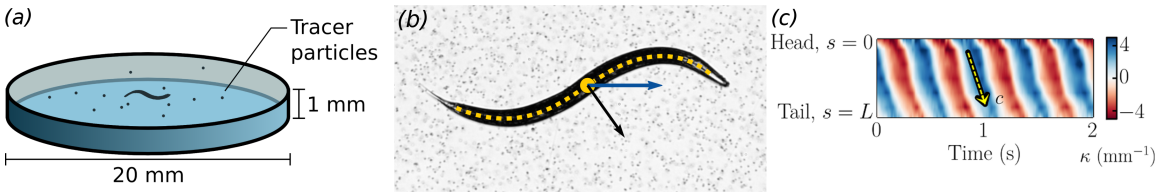

Figure 1: *(a)* Schematic of nematode *C. elegans* swimming in a sealed fluidic chamber. *(b)* *C. elegans* swimming through fluid seeded with tracer particles. Yellow line show instantaneous body shape, black arrow defines an outward normal vector and blue arrow shows the direction of motion. *(c)* Nematode's body curvature during swimming. Curvature plot for approximately four beating cycles illustrates characteristic traveling wave propagating from head to tail. Wave speed c is highlighted by the yellow dashed arrow.

et al., 1986). Their neuromuscular system controls their body undulations, allowing *C. elegans* to swim, dig, and crawl through diverse environments. The wealth of biological knowledge accumulated to date makes *C. elegans* an ideal candidate for investigations that combine aspects of biology, biomechanics, and the fluid mechanics of propulsion.

We place nematodes into sealed fluidic chambers (Fig. 1*(a)*) that are 2 cm in diameter and 1 mm in depth, and image their swimming motion using standard bright-field microscopy (Infinity K2/SC microscope with an in-system amplifier, a CF-3 objective, and an IO Industries Flare M180 camera at 150 frames per second). The depth of focus of the objective is approximately 20 µm and the focal plane is set on the longitudinal axis of the nematode body. The nematode beats primarily in the observation plane; the out-of-plane beating amplitude of *C. elegans* is less than 6% of the amplitude of its in-plane motion (Sznitman et al., 2010b). All data presented here pertain to nematodes swimming at the center of the fluidic chamber and out-of-plane recordings are discarded to avoid nematode-wall interactions and to minimize three-dimensional flow effects.

1.6. Swimming kinematics

The nematode's swimming kinematics are obtained from videos using in-house software (Sznitman et al., 2010c). The software extracts the nematode's centroid position and body shape-

line, and computes quantities such as swimming speed U and body curvature κ. Swimming speed is obtained by differentiating the nematode's centroid position with time, and we define the positive y-axis as the swimming direction (see figure 1*(b)*). The body curvature is defined as $\kappa = \delta\phi/\delta s$, where ϕ is the angle between a fixed reference axis and the tangent to the body shape-line, at each point s along the body contour, where s is an arc length parameterization. Figure 1*(c)* shows the evolution of $\kappa(s,t)$ for approximately four beating cycles, revealing periodic lines that propagate in time from head ($s = 0$) to tail ($s = L$), illustrating the characteristic traveling wave of undulatory swimming. The slope and rate of occurrence of these lines represent wave speed c (figure 1*(c)*, yellow dashed line) and beating frequency f, respectively. In water-like buffer solutions, we find $U \approx 0.35$ mm/s, $f \approx 2$ Hz, and $c \approx 5$ mm/s. The Reynolds number, defined as $Re = \rho UL/\eta$, is approximately 0.35, where L is the nematode's length (1 mm), ρ is the fluid's density (10^3 kg/m^3), and η is the fluid's viscosity (1 mPa·s), indicating that viscous forces dominate the flow. The range of Reynolds numbers for all experiments is $10^{-4} < Re \leq 0.35$.

1.7. Particle tracking

We measure the velocity fields generated by swimming *C. elegans* in both Newtonian and non-Newtonian fluids by seeding the working fluids with 3.1 µm polystyrene tracer particles, which are tracked continuously for the entire duration of the experiment using in-house codes. These tracer particles are dilute ($< 0.5\%$ by volume) and do not alter the properties of the fluid. We image the nematodes swimming through this seeded fluid for 6 to 10 cycles, with each swimming cycle (or period) containing 60 phases. Because *C. elegans* beat at a constant frequency, we can phase-average the data and obtain spatially resolved velocity fields. We note that data points for each phase are averaged into gridded spaces of approximately 20 µm.

CHAPTER 2 : A fluid dynamics perspective of biological locomotion

The study of microorganism and cell swimming has numerous applications in both industry and medicine, for instance in the context of mammalian reproduction (Johnson et al., 1999; Fauci and Dillon, 2006), biofuel production (Bees and Croze, 2014), and the design of artificial biomedical systems (Qiu and Nelson, 2015). Many of these swimmers, such as mammalian spermatozoa, self-propel by generating traveling undulations along their body (Lauga and Powers, 2009; Gaffney et al., 2011). One such undulatory swimmer is the biological model organism *Caenorhabditis elegans*, a multi-cellular, free-living slender nematode worm found in soil environments.

Recently, *C. elegans* has been used extensively as a model system for experimental studies of propulsion, particularly at low Reynolds number, due to its simple planar swimming gait and size (Gray and Lissmann, 1964; Korta et al., 2007; M.Backholm et al., 2014; Shen and Arratia, 2011; Bilbao et al., 2013; Gagnon et al., 2014a; Park et al., 2016). The nematode generates planar bending waves through contractions of its ventral and dorsal muscles, producing a quasi-two-dimensional (2D) traveling sinewave along its body (Korta et al., 2007; Sznitman et al., 2010b; Thomases and Guy, 2014b). At around 1 mm in length and 75 µm in diameter, *C. elegans* is significantly larger than the majority of low-Re undulatory swimmers, enabling high-resolution reconstruction and analysis of planar flow fields from particle tracking data. The resulting flow-fields can be used to probe properties of both the swimmer and fluid, providing new insights into the physics of undulatory propulsion (Shen and Arratia, 2011; Gagnon et al., 2013; M.Backholm et al., 2014; Majumdar et al., 2012; Bilbao et al., 2013; Gagnon et al., 2014a; Yuan et al., 2015; Park et al., 2016).

However, despite exhibiting a planar swimming stroke, the flow around *C. elegans* has a complex three-dimensional structure, which is difficult to capture experimentally. Many useful flow properties, such as the shear rate, are dependent upon out-of-plane flow con-

tributions not measured by planar velocimetry data; in essence, one measures a 2D slice of a three-dimensional (3D) field. This limits, for example, our ability to accurately determine drag and propulsion forces experienced and exerted by the swimming nematode. In this work, we show that numerical and theoretical fluid mechanics techniques can be used to improve the processing and analysis of these experimental flow-fields.

We first obtain detailed (experimental) imaging data on the shape and kinematics of a swimming *C. elegans*, together with particle-tracking data for flow-field reconstruction. We then collaborated with Thomas Montenegro-Johnson and Eric Lauga to develop a numerical boundary element model of the nematode, with geometry and boundary conditions specified directly from the experiments, and use this model to improve the processing of particle tracking velocimetry results. Using simulated flow-fields, we examine the spatial distribution of flow shear rate, an important quantity related to power dissipation and relevant for studies on locomotion in complex, shear-dependent fluids. We show that using purely planar data significantly underestimates the true value of the shear rate throughout the field. We then use symmetry arguments validated against numerics to show that the 2D measurements can be corrected for out-of-plane effects by applying the incompressibility constraint. Our work shows that fundamental fluid mechanics tools can be used alongside experimental measurements to improve our understanding of the biomechanics of locomotion.

2.1. Methods

We first describe the technical improvements carried out in this work. In order to compare the results of the numerical model directly with our experimental data, we use the same swimming movie to construct experimental velocity fields and to obtain the motion of the nematode, which provides the nematode's geometry and kinematics for the numerical simulations.

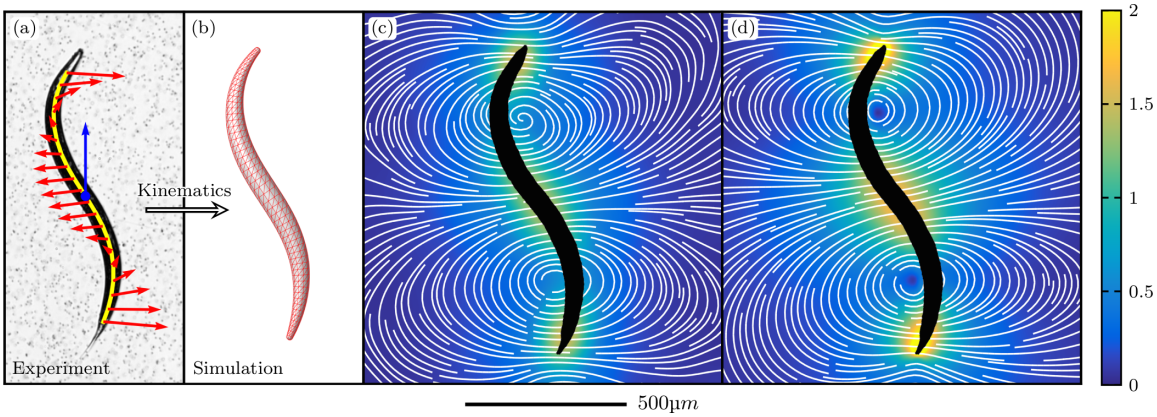

Figure 2: *(a)* Image of the nematode *C. elegans*. The yellow line shows the "skeletonized" body, and the red arrows denote the velocities of each body-segment. The blue arrow indicates the swimming direction. *(b)* Three-dimensional mesh constructed from the experimentally-obtained body-shape and kinematics of the nematode for the same snapshot. *(c)* Experimentally-measured streamlines for one snapshot of swimming *C. elegans*, produced using particle tracking velocimetry techniques. *(d)* Flow-field produced using the reconstructed 3D mesh and a numerical model for the same snapshot. Color bar: speed mm/s.

Particle tracking procedures around swimmers entail a delicate balance between maximizing the quantity of statistics from which to construct a velocity field, and the precision of those measurements. For *C. elegans*, one needs enough statistics to construct a smooth, differentiable velocity field, yet the most precise particle tracking data is located strictly at the nematode z-mid-plane (direction across the depth of field). Additionally, due to the fact that our microscope objectives have a depth of field of approximately 20 µm, our experiments represent a *depth-averaged* 2D slice of a 3D flow-field over this thickness.

Here, the simulation provides benchmark flow-fields, allowing greater selectivity for our particle identification and tracking algorithms. This selection ensures that we only choose particles close to the z-mid-plane, shifting the balance from maximizing the number of statistics to maximizing the precision of our measurements. In regions where we have limited data, we use gentle maximum value and bilateral filtering algorithms to smooth our experimental results so that they can be differentiated.

2.1.1. Data acquisition and processing

Experiments with *C. elegans* are performed in Newtonian, water-like ($\mu \approx 1\,\mathrm{mPa}\cdot\mathrm{s}$ and $\rho \approx 10^3\,\mathrm{kg/m^3}$) M9 buffer solutions (Brenner, 1974) in a sealed fluid chamber 20 mm in diameter and 1 mm in depth. Images are captured using standard bright-field microscopy (Infinity K2/SC microscope with a CF-4 objective, and an IO Industries Flare M180 camera at 150 frames per second). The depth of focus of the objective is approximately 20 µm, and we ensure that the focal plane is in the middle of the chamber in order to minimize wall effects. The nematode beats primarily in the observation plane; the out-of-plane beating amplitude is less than 6% of its in-plane motion, and therefore confinement effects are minimal (Sznitman et al., 2010b). Given that the flow decay is expected to be exponential, we also anticipate negligible influence of the chamber boundaries on the flow field (see Fig. 4) (Lighthill, 1976). All data presented here pertain to nematodes swimming at the centre of the fluidic chamber and out-of-plane recordings are discarded to avoid nematode-wall interactions and to minimize three-dimensional flow effects.

In-house software is used to track the swimming motion of *C. elegans*. The position of the nematode's centroid is differentiated with respect to time to obtain swimming speed ($U \approx 0.3$ mm/s), the head position is used to compute an average amplitude ($A \approx 0.25$ mm), and a comparison of periodic body shapes is used to estimate the nematode's beating frequency ($f \approx 2$ Hz). Beyond average kinematic properties, the nematode body contour is automatically extracted for each image frame, skeletonized (yellow line in Fig. 2*a*), and divided into segments that are tracked to obtain local body velocities. Sample velocity vectors of the body are shown in Fig. 2*a* in red. This body shape and associated velocities are used to create an approximate 3D model of the nematode and its surface velocities, as illustrated in Fig. 2*b*.

Particle tracking velocimetry is used to measure the velocity fields generated by swimming *C. elegans*. In short, we seed the chamber with 3 µm polystyrene tracer particles (Fig. 2*a*)

that are tracked using with in-house algorithms. We track the flow for approximately 8 beat-cycles, and divide each cycle into approximately 50 phases. Because the nematode's swimming stroke is highly periodic ($\sim$ 2 Hz) (Sznitman et al., 2010b), we can construct a "master" swimming cycle using a least-squares fit of the nematode's body shapes. This phase-averaging technique considerably improves the spatial resolution of the experimental velocity fields. In order to estimate the flow-field around the nematode's body more accurately, we include velocities within the contour of the the swimmer-fluid interface, assuming a no-slip boundary condition. Finally, the data points for each phase, including tracking plus boundary conditions, are averaged into gridded spaces of size 13.2 µm. The resulting experimental streamlines are illustrated in Fig. 2*c* for one particular phase.

2.1.2. Numerical model

In this section, we describe the numerical model developed by our collaborators Thomas Montenegro-Johnson and Eric Lauga for comparison to our experimental results (Montenegro-Johnson et al., 2016). *C. elegans* moves through a water-like Newtonian buffer solution (Brenner, 1974) and the dynamics of the flow driven by the swimming nematode is well-modeled by the Stokes flow equations

$$\mu\nabla^2\mathbf{u} - \nabla p = 0, \quad \nabla\cdot\mathbf{u} = 0, \tag{2.1}$$

where $\mathbf{u}$ is the fluid velocity and p the dynamic pressure.

In order to solve Eqs. (2.1) in the fluid surrounding the nematode, we employ the regularized stokeslet boundary element method (Cortez et al., 2005; Smith, 2009). The velocity throughout the domain is given by integrals of stokeslets $\mathbf{S}$ and stresslets $\mathbf{T}$ over the nema-

tode's surface, S

$$\lambda u_j(\mathbf{x}_0) = \int_S S^\epsilon_{ij}(\mathbf{x},\mathbf{x}_0) f_i(\mathbf{x}) - u_i(\mathbf{x}) T^\epsilon_{ijk}(\mathbf{x},\mathbf{x}_0) n_k(\mathbf{x})\, \mathrm{d}S_x, \tag{2.2}$$

for unknown surface tractions, $\mathbf{f}$, and surface velocity $\mathbf{u}$ specified from experimental data (Montenegro-Johnson et al., 2016).

Note that in the majority of implementations of the method of regularised stokeslets, the stresslet "double-layer" $u_i(\mathbf{x}) T^\epsilon_{ijk}(\mathbf{x},\mathbf{x}_0) n_k(\mathbf{x})$ term in equation (2.2) is eliminated, and the constant $\lambda = 1$ (Pozrikidis, 1992). However the surface tractions solved for in the simplified "single layer" formulation are a modified force density dependent upon a fictitious "complementary" flow inside the worm. In order to provide a general method that might in the future be used to examine the energetics of locomotion and force generation inside the worm, the full formulation is used (Montenegro-Johnson et al., 2016).

In our case, the constant λ is given at leading order by $\lambda \approx 1/2 + \kappa\epsilon/4$, where κ is the mean local curvature of the surface at $\mathbf{x}_0$ (Montenegro-Johnson et al., 2015). We use the regularized form of the stokeslet S^ϵ_{ij} and stresslet T^ϵ_{ijk} (Cortez et al., 2005),

$$S^\epsilon_{ij}(\mathbf{x},\mathbf{x}_0) = \frac{\delta_{ij}(r^2 + 2\epsilon^2) + r_i r_j}{r_\epsilon^3}, \tag{2.3a}$$

$$T^\epsilon_{ijk}(\mathbf{x},\mathbf{x}_0) = -\frac{6 r_i r_j r_k}{r_\epsilon^5} - \frac{3\epsilon^2\left(r_i\delta_{jk} + r_j\delta_{ik} + r_k\delta_{ij}\right)}{r_\epsilon^5}, \tag{2.3b}$$

derived from a regularisation of the dirac delta function of the form

$$\phi_\epsilon(\mathbf{x} - \mathbf{x}_0) = \frac{15\epsilon^4}{8\pi r_\epsilon^7}, \quad r_\epsilon^2 = r^2 + \epsilon^2, \tag{2.4}$$

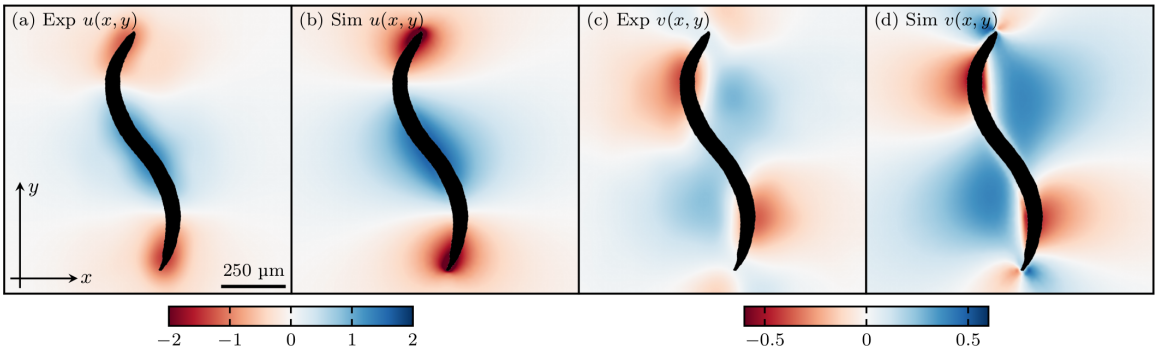

Figure 3: Spatial distribution of the (a) experimentally-measured x-component $u(x,y)$, (b) simulated x-component, (c) experimentally-measured y-component $v(x,y)$, and (d) simulated y-component. Experimental measurements demonstrating good agreement with simulation. Color bars: component velocity magnitude mm/s.

where $r_i = (\mathbf{x} - \mathbf{x}_0)_i, r = |\mathbf{x} - \mathbf{x}_0|$ and $\epsilon \ll 1$ (with $\epsilon = 10^{-4}L$ in our simulations). The implementation uses routines adapted from BEMLIB (Pozrikidis, 2002) and Thomas Montenegro-Johnson's boundary element library RegBEM Phoretic (Montenegro-Johnson et al., 2016), which employs a linear panel representation of the unknown surface tractions $f_i(\mathbf{x})$ with adaptive Fekete quadrature for near-singular element integrals (Montenegro-Johnson et al., 2015, 2016).

The nematode geometry is meshed with piecewise-quadratic triangular elements (Fig. 2*b*) using a custom routine which extrudes a circle of radius $a(s)$ along the experimentally-captured nematode centerline, and caps the head and tail of the worm with a section of a sphere. The radius $a(s)$ is given as a function of arc-length s by fitting a quadratic through the nematode's radius at the midpoint a_1 and the head a_2, so that for a nematode of length L we have

$$a(s) = \frac{4(a_2 - a_1)}{L^2}\left(s - \frac{L}{2}\right)^2 + a_1. \tag{2.5}$$

The velocity boundary condition (no-slip) is then imposed on the mesh surface directly from experimental data via time-centered finite differences of the nematode centerline (Montenegro-Johnson et al., 2016).

2.2. Results and Discussion

2.2.1. Comparison of experiments and simulations

Fig. 2 shows the streamlines computed experimentally using particle tracking velocimetry *(c)* and numerically using simulated flow-fields *(d)*. These streamlines show strong agreement, with both methods capturing head and tail vortices of similar shape and size. A visual comparison of the x- and y-components of the velocity field, u and v respectively, again shows very good agreement between experiment and simulation (Fig. 3). In order to quantify this comparison, Fig. 4*(a,b,c)* shows the distributions of velocity components u and v and speed $|\mathbf{u}|$ for experimental and simulated fields. These plots show that the experiments capture the majority of velocities, with the exception of the highest velocities corresponding to points closest to the nematode, where it is difficult to obtain accurate particle tracks. Experiments also predict a larger proportion of zero velocities, which is again associated with the difficulty of extracting smooth, small, but non-zero, velocities from noisy particle data.

Finally, we calculate the spatial decay of the flow speed away from the body of the swimmer. For an undulatory swimmer, we expect to observe an exponential flow decay (Lighthill, 1976),

$$\frac{|\mathbf{u}|}{|\mathbf{u}_b|} = \exp\left(-\frac{2\pi r}{\alpha L}\right), \tag{2.6}$$

where $|\mathbf{u}|$ is a velocity measurement, $|\mathbf{u}_b|$ is the speed of the swimmer's body, assuming a no-slip boundary condition, r is the normal distance from each velocity measurement to the swimmer's body, L is a characteristic length-scale of the swimmer (we take $L \approx$ 1 mm), and α is an exponential parameter that specifies the rate of decay. We find that the simulations and experiments are in good agreement with $\alpha_{\text{exp}} = 0.74$ and $\alpha_{\text{sim}} = 0.85$, showing a difference of just 13% in the exponent (Fig. 4, last panel).

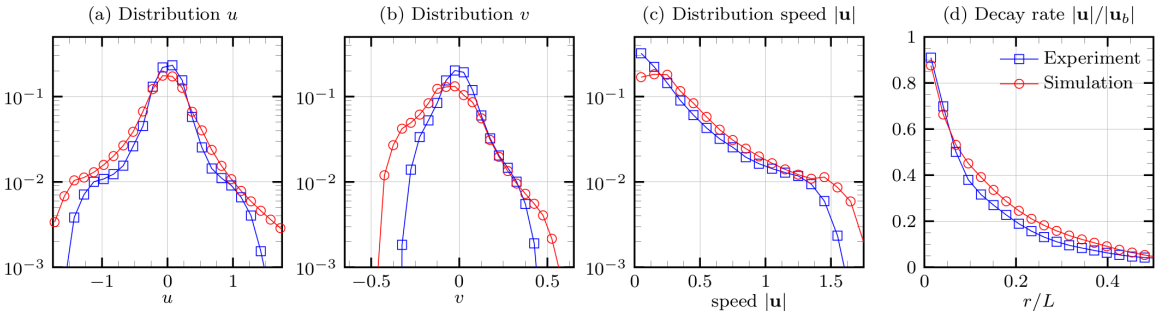

Figure 4: Comparison of flow structure between experiment and simulation: (a) distribution of u, (b) distribution of v, (c) distribution of speed $|\mathbf{u}|$, and (d) decay rate $|\mathbf{u}|/|\mathbf{u}_b|$.

2.2.2. *Shear rate calculation and correction*

A particularly salient characteristic of the flow-field is the spatial ditribution of shear rate, $\dot{\gamma} = \sqrt{\boldsymbol{\varepsilon}(\mathbf{u}) : \boldsymbol{\varepsilon}(\mathbf{u})/2}$ with $\boldsymbol{\varepsilon}(\mathbf{u}) = \boldsymbol{\nabla}\mathbf{u} + \boldsymbol{\nabla}\mathbf{u}^T$, which is important for calculation of power dissipation, the energetics of locomotion, and is also relevant for studies on locomotion in complex, (shear) rate-dependent fluids. Since the beat-pattern of the nematode is planar, there is no flow in the z-direction in the swimmer mid-plane. However the z-derivatives of the mid-plane velocity will make, in general, non-trivial contributions to the shear rate. Writing the shear rate in 2D and 3D explicitly, we see

$$\dot{\gamma}_{2D} = [2u_x^2 + (u_y + v_x)^2 + 2v_y^2]^{1/2}, \tag{2.7a}$$

$$\dot{\gamma}_{3D} = [2u_x^2 + (u_y + v_x)^2 + 2v_y^2 + 2w_z^2 + (u_z + w_x)^2 + (v_z + w_y)^2]^{1/2}, \tag{2.7b}$$

where u, v, w are the x, y, z components of the velocity field, and subscripts denote derivative components.

Because of the additional terms in the 3D formula, we expect calculation of the shear rate from 2D particle tracking flow-fields will likely result in a systematic underestimate of the true 3D value. Fig. 5*a* shows that this is indeed the case; the spatial distribution of the

relative percentage error in the simulated shear rate calculated with the 2D formula (2.7a) compared with the true 3D value spatial distribution of the shear rate as calculated by the 3D (2.7b) is significant, even reasonably far from the worm, and is around 30% close to the worm. Indeed the integrated root mean square error in this field is 14%. Thus, we see that we have significant errors throughout the field, but particularly close to the worm where calculations of shear rate are of particular interest.

We wish to correct for this error without resorting to Boundary Element calculations, and so require estimates of the unknown quantities in the 3D formula (2.7b). Since the worm kinematics is planar, we have the symmetry $z \to -z$, and so there is no z-flow in the mid-plane and the quantities w_x and w_y are zero. Furthermore, the quantities u_z and v_z are also zero by this symmetry. These observations are confirmed by our numerical simulation, which calculates the above quantities to be zero within numerical error. However, the z-component of the velocity w changes sign through the mid-plane, and thus its z-derivative w_z makes a significant contribution to the shear rate. The 3D formula (2.7b) can thus be simplified,

$$\dot{\gamma}_{\text{pl}} = [2u_x^2 + (u_y + v_x)^2 + 2v_y^2 + 2w_z^2]^{1/2}. \tag{2.8}$$

Since the flow is incompressible, we have $\boldsymbol{\nabla} \cdot \mathbf{u} = 0$, so that $w_z = -(u_x + v_y)$, giving the final formula

$$\dot{\gamma}_{\text{pl}} = [2u_x^2 + 2v_y^2 + (u_y + v_x)^2 + 2(u_x + v_y)^2]^{1/2}, \tag{2.9}$$

purely in terms of planar components obtainable via planar particle tracking. Applying the adjusted formula (2.9) to our numerical data, the error is eliminated to within 0.01% which is attributable to the accuracy of our numerical scheme.

The principal advantage of this approach is that it can be applied in just as simple a manner to incompressible non-Newtonian flows, such as shear-thinning and viscoelastic fluids. Such fluids have complex non-Newtonian constitutive laws, and do not readily admit

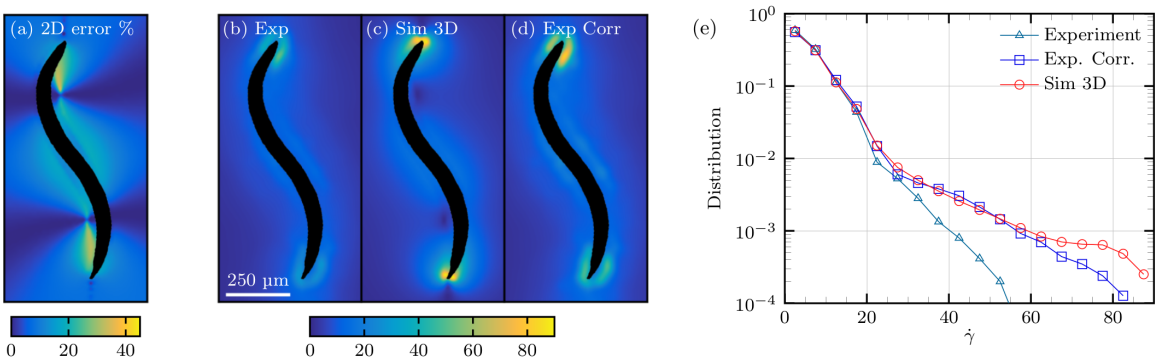

Figure 5: Shear rate error, calculation, and correction: (a) The percentage relative error in the shear rate as calculated using the 2D formula (2.7a) for simulated data, showing large errors throughout. (b)-(d) Shear rate field for (b) planar 2D experiments calculated with the 2D formula (2.7a), (c) 3D simulation calculated with the full formula (2.7b), and (d) corrected "3D" experiments calculated with the corrected formula (2.9). (e) Distribution of shear rates for planar experiments, 3D simulation, and corrected experiments. Note the marked improvement in similarity between shear rate distribution for the corrected experiments and that of the full 3D simulation.

simple three-dimensional simulation.

We now directly compute the 2D (2.7a) and the estimated 3D (2.9) shear rate field for our experimental data (Fig. 5*b*). Figure 5 shows a comparison between the "corrected" 3D shear rate field from experiments and the 3D shear rate field from simulations *(c,d)*. We find the corrected field from experiments and the simulated 3D field have a strikingly similar structure and an RMS error of only 14%, compared to an RMS error of roughly 20% before the correction was applied. We note, however, that there are discrepancies near the head and tail of the worm, where the simulations suggest a slightly higher shear rate ($\approx$ 10%); these regions of high velocity near the swimmer-fluid interface are in locations where we expect particle tracking techniques to pose the greatest challenge.

To quantify the differences between the shear rate fields of the simulations and experiments, as well as demonstrate the effectiveness of our correction factor for 2D data, we show the distribution of shear rate for the raw experimental data, corrected experimental data, and the full 3D simulations (Fig. 5*e*). We find that a 2D calculation of shear rate using

our experimental data underestimates shear rate for values of $\dot{\gamma} > 25\ \mathrm{s}^{-1}$ compared to the 3D simulated shear rate field. When the Eq. 2.9 is applied to the experimental data, we capture the same shear rate distribution as the 3D simulations up to $\dot{\gamma} = 60\ \mathrm{s}^{-1}$. For larger shear rates ($\dot{\gamma} > 60\ \mathrm{s}^{-1}$), we see only minor deviations from the 3D simulations, suggesting that the corrected shear rate field significantly improves our ability to estimate the shear rate magnitude from planar data.

Since the shear rate is calculated using derivatives of the velocity field, small fluctuations or errors in the velocity field are magnified substantially. Nonetheless, we obtain good agreement between experiment and simulation, with errors being confined to regions of high shear rate; importantly, we find that the application of the analytical correction factor greatly improves our estimate of the maximum shear rate around the swimmer, which is particularly useful for swimming applications with non-Newtonian fluids. These results indicate that the local shear rate near a low Reynolds number swimmer is likely much higher than previously thought, due to contributions in the third dimension that planar particle tracking velocimetry does not directly measure. As a result, non-Newtonian effects as a result of locomotion in complex fluids may be much larger than anticipated. Examples include the role of elastic stretching, measured by the Weissenberg number $Wi = \lambda_E \dot{\gamma}$ where λ_E is the longest relaxation time of the fluid, and shear-thinning viscosity behavior, measured by the Carreau number $Cr = \lambda_{Cr} \dot{\gamma}$ where λ_{Cr} is a timescale that represents the onset of shear-thinning effects; our accounting for the shear rate in the third dimension therefore suggests that a planar experimental measurement may underrepresent non-Newtonian effects near the body of a the swimmer.

2.3. Summary

In this work, we used theoretical and numerical techniques to improve the processing of experimentally obtained particle tracking data, producing smooth velocity fields quantifying the flow around the swimming nematode *C. elegans* in a Newtonian solution. We com-

pared our results with a 3D boundary element model of the nematode, generated directly from experimentally obtained nematode kinematics, finding good agreement between numerics and experiment.

We argued that when calculating derivative flow quantities, the only non-trivial out-of-plane component is w_z: the z-derivative of the z-flow. This observation was validated by simulation, showing that excluding w_z when calculating the flow shear rate results in a significant underestimate. Accounting for the w_z component via incompressibility from 2D data eliminated this error.

Our work illustrates how theory may be used to improve experimental measurements in biological fluid mechanics, and will be directly applicable to investigations of bio-locomotion in complex fluids. Furthermore, we anticipate that as technology for the acquisition and processing of experimental flow-fields continues to improve, these out-of-plane effects will represent a hard barrier to increasing the accuracy of results, making such techniques increasingly important.

CHAPTER 3 : Swimming in shear-thinning fluids

Recently, there has been much interest in understanding the swimming behaviour of microorganisms at low *Re* in simple, Newtonian fluids (Lauga and Powers, 2009; Guasto et al., 2010; Saintillan and Shelley, 2012; Lauga and Goldstein, 2012). However, many organisms swim in non-Newtonian environments such as mucus, blood, and soil (Harman et al., 2012; Alexander, 1991). An important feature of non-Newtonian fluids is that they often exhibit viscoelasticity and shear-rate dependent viscosity. While much work has been devoted to the effects of fluid elasticity on the swimming of microorganisms (Lauga, 2007; Fu et al., 2009, 2010; Teran et al., 2010; Shen and Arratia, 2011; Liu et al., 2011), there are relatively few studies of swimming in shear-thinning fluids.

To date, major studies of the effects of shear-thinning viscosity have been theoretical (Vélez-Cordero and Lauga, 2013) and numerical (Montenegro-Johnson et al., 2012, 2013). The theoretical analysis focused on a two-dimensional, infinite waving sheet immersed in a model Carreau (shear-thinning) fluid, and found a non-Newtonian contribution to propulsion speed to fourth order in amplitude when the sheet was extensible, but no non-Newtonian contribution to propulsion speed when an inextensible condition was applied (Vélez-Cordero and Lauga, 2013). Additionally, this analysis suggested the cost of transport was reduced and the flow field was modified, with increased vorticity near the sheet. Additionally, for a finite swimmer, this analysis suggested the cost of transport was reduced and the flow field was modified, with increased vorticity near the sheet (Vélez-Cordero and Lauga, 2013). Separate simulations (Montenegro-Johnson et al., 2012, 2013) also using the Carreau model suggested that undulatory swimmers with a head or "payload" (similar to a sperm cell) are assisted by shear-thinning viscosity, resulting in increased speed and that the swimmer's motion results in an envelope of thinned fluid around the body.

Despite these recent and important efforts, there is still a dearth of experimental investi-

gations of swimming in shear-thinning fluids, and the effects of rate-dependent viscosity on swimming remain unclear. Experiments with a mechanical model system (Dasgupta et al., 2013) finds a decrease in propulsion for fluids possessing both shear-thinning and viscoelastic behavior, while the swimming speed of *C. elegans* is shown to be unaffected by shear-thinning viscosity (Shen and Arratia, 2011) although only a single data point is available. Here, we experimentally investigate the effects of shear-thinning viscosity on the swimming behaviour of a model biological organism, the nematode *Caenorhabditis elegans*. The nematode's position and swimming stroke is tracked using in-house software (Sznitman et al., 2010c) and flow fields are obtained using particle tracking methods (Sznitman et al., 2010b). Results show there is no change in the nematode's kinematics due to shear-thinning effects. Yet with this unchanged swimming stroke, the nematode in shear-thinning fluid generates a remarkably different flow field, with enhanced vorticity and an altered spatial pattern of fluid velocity. We compare these experimental results to recent analysis (Vélez-Cordero and Lauga, 2013) and numerical simulations (Montenegro-Johnson et al., 2012, 2013).

3.1. Fluid rheology

We use both Newtonian and shear-thinning fluids in this investigation. The range of Reynolds numbers, defined as $Re = \rho UL/\eta$, is $10^{-4} < Re \leq 0.35$ across all experiments, where $Re = 0.35$ represents the water-like case. For shear-thinning fluids, we use η measured at the estimated mean strain rate (from velocity fields) in computing the Re, which defines the fluid effective viscosity η_{eff} in our experiments. We could alternately use the zero-shear-rate viscosity η_0 instead, but this choice would underestimate Re. Since the non-Newtonian fluid viscosity is rate-dependent, the use of the mean strain-rate to estimate η seems appropriate.

We prepare Newtonian fluids to cover a range of viscosities, ranging from 1 mPa·s to 700 mPa·s. From lowest to highest viscosity, we use *(i)* a water-like buffer solution (M9

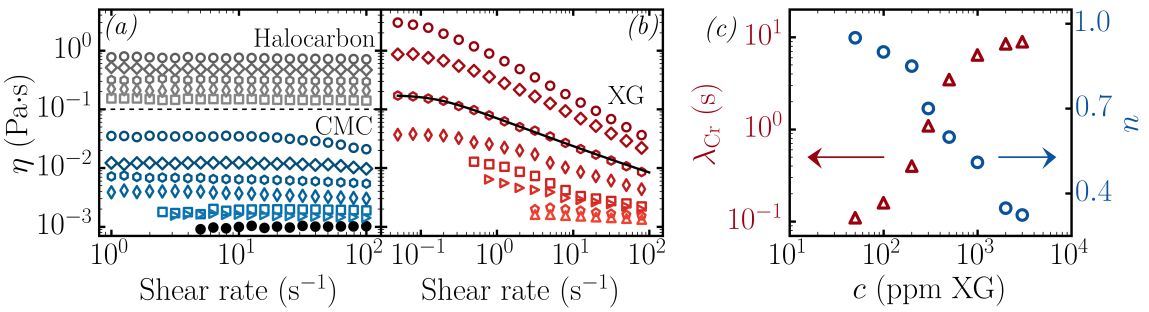

Figure 6: *(a)* Measurements of viscosity η as a function of shear rate $\dot{\gamma}$ for the Newtonian buffer solution M9 (closed symbols), CMC solutions in M9 (blue open symbols, concentrations from bottom to top: 300, 500, 1000, 1500, 2000, and 3000 ppm, Sznitman et al. (2010b)), and halocarbon oil mixtures (grey open symbols, from bottom to top: 100% H27, 44% H700, 61% H700, 78% H700, and 95% H700 by weight, Shen and Arratia (2011)). *(b)* Measurements of viscosity η as a function of shear rate $\dot{\gamma}$ for shear-thinning solutions of XG in M9 (from bottom to top: 50, 100, 200, 300, 500, 1000, 2000, and 3000 ppm). The solid black line shows a fit to the Carreau-Yasuda model (Eq. 3.1) *(c)* Carreau timescale λ_{Cr} as a function of concentration (△) and power law index n (○) as a function of concentration c_{XG}.

salt solution) (Brenner, 1974), *(ii)* very dilute solutions of the polymer carboxymethyl cellulose in M9 salt solution (CMC, 7×10^5 MW, Sigma Aldrich 419338), and *(iii)* mixtures of two molecular weights of chlorotrifluoroethylene (halocarbon oils H27 and H700; Sigma Aldrich H8773 and H8898, respectively) (Sznitman et al., 2010b). We note that halocarbon oil mixtures are limited to only Newtonian swimming kinematics data due to a significant density mismatch between these polymer solutions and polystyrene tracer particles. The polymer CMC possesses a flexible backbone, and (aqueous) solutions of CMC may exhibit viscoelasticity. Here, however, we minimize the effects of elasticity by using a low polymer concentration ($c_{CMC} \lesssim 10^3$) in comparison to the overlap concentration $c^*_{CMC} = 10^4$ in addition to the presence of salt (M9) (Sznitman et al., 2010b). As a result, these solutions exhibit negligible shear-thinning rheology and elasticity (Shen and Arratia, 2011), and sample rheology curves for CMC solutions are given in Fig. 6*(a)*.

We prepare shear-thinning fluids by adding small amounts of the polymer xanthan gum (XG, 2.7×10^6 MW, Sigma Aldrich G1253) to water in the presence of salt. The XG concen-

tration in buffer ranges from 50 ppm to 3000 ppm. These aqueous XG solutions have been well characterized and are known to have negligible elasticity (Shen and Arratia, 2011; Gagnon et al., 2014a). We characterize all fluids (Newtonian and shear-thinning) using a cone-and-plate rheometer (strain-controlled RFS III, TA Instruments) at a range of constant shear rates. Fig. 6*(a)* and Fig. 6*(b)* show the fluid viscosity η as a function of shear rate measurements for Newtonian and shear-thinning fluids, respectively. We find strong shear-thinning behavior (e.g. power law viscosity) for the most concentrated XG solution ($c_{\mathrm{XG}} = 3000$ ppm), and this shear-thinning behavior gradually decreases as the concentration of XG decreases; at the lowest concentration ($c_{\mathrm{XG}} = 100$ ppm), the behavior of the XG solutions is Newtonian-like. We quantify this shear-thinning viscosity by fitting the rheological data with the Carreau-Yasuda model (Carreau et al., 1997):

$$\eta\left(\dot{\gamma}\right) = \eta_{\infty} + \left(\eta_0 - \eta_{\infty}\right)\left(1 + \left(\lambda_{Cr}\dot{\gamma}\right)^2\right)^{\frac{n-1}{2}}, \tag{3.1}$$

where $\eta\left(\dot{\gamma}\right)$ is the fluid's shear rate-dependent viscosity, $\dot{\gamma} = |\dot{\boldsymbol{\gamma}}| \equiv \sqrt{\frac{1}{2}\left(\dot{\boldsymbol{\gamma}} : \dot{\boldsymbol{\gamma}}\right)}$ is the magnitude of the shear rate tensor $\dot{\boldsymbol{\gamma}} \equiv \frac{1}{2}\left(\boldsymbol{\nabla u} + \boldsymbol{\nabla u}^{\mathsf{T}}\right)$, η_0 is the zero-shear viscosity, η_{∞} is the infinite-shear viscosity, and n is the power-law index.

The characteristic timescale λ_{Cr} represents the inverse of the shear rate at which the fluid transitions from Newtonian-like to power-law behavior; values of λ_{Cr} for each fluid are shown in Fig. 6*(c)*. Larger timescales indicate that the fluid exhibits shear-thinning properties at lower shear rates (Carreau et al., 1997). Using this timescale, we can define a non-dimensional shear rate based on the kinematics of the nematode. This kinematic Carreau number describes the strength of the shear-thinning behavior, and we define it as $Cr_k = 2\pi\lambda_{Cr} f A k$, where f is the beating frequency, A is the average beating amplitude, and k is the wave number of the swimming nematode (Li and Ardekani, 2015). A fluid behaves Newtonian-like when $Cr_k \ll 1$ with a viscosity $\eta \approx \eta_0$. When $Cr_k \gtrsim 1$, the fluid exhibits shear-thinning behavior. The power-law index n, shown in Fig. 6*(c)*, describes the

sensitivity of the fluid's viscosity to changes in shear rate.

3.2. Swimming Kinematics

First, we investigate the swimming kinematics of nematodes in Newtonian and shear-thinning fluids. Figure 7*(a-f)* show the nematode's *(a)* swimming speed U, *(b)* beating frequency f, *(c)* beating amplitude A, *(d)* wave speed c, *(e)* Strouhal number $St = fA/U$, and *(f)* kinematic efficiency U/c as a function of effective viscosity η_{eff} for both Newtonian and shear-thinning fluids. Note that for shear-thinning fluids, η_{eff} is defined as the average viscosity over a characteristic range of shear rates, $U/L \leq \dot{\gamma} \leq 2fA/d$. The rate $U/L \sim 0.35$ s^{-1} describes the forward progress of the entire nematode, and the rate $2fA/d \sim 15$ s^{-1} describes the nematode's local transverse motion, where $d/2 \sim 40$ µm is the body radius. These estimates are in good agreement with measured shear rates.

The data in figure 7 show that the nematode's swimming kinematics in shear-thinning fluids are very similar to those in Newtonian fluids of the same effective viscosity. This suggests that the nematode's kinematics are responding solely to bulk viscous effects and not local shear-thinning effects. For example, the nematode's swimming speed U (figure 7*(a)*) is approximately constant for both shear-thinning and Newtonian fluids up to $\eta_{eff} \approx 50$ mPa·s. A decrease in U is also found for both shear-thinning and Newtonian fluids for $\eta_{eff} > 50$ mPa·s, which is in agreement with the power-limited nature of *C. elegans* (Shen and Arratia, 2011).

Overall, we find no evidence that shear-rate-dependent viscosity influences the swimming stroke or speed of *C. elegans*. Our findings seem to be in agreement, at least in part, with a recent theoretical work (Vélez-Cordero and Lauga, 2013), in which the authors find no shear-thinning-induced changes to swimming speed for an inextensible sheet. For an extensible sheet, the same study finds an increase in swimming speed in shear-thinning fluids. We note, however, that there are differences between our experimental system and

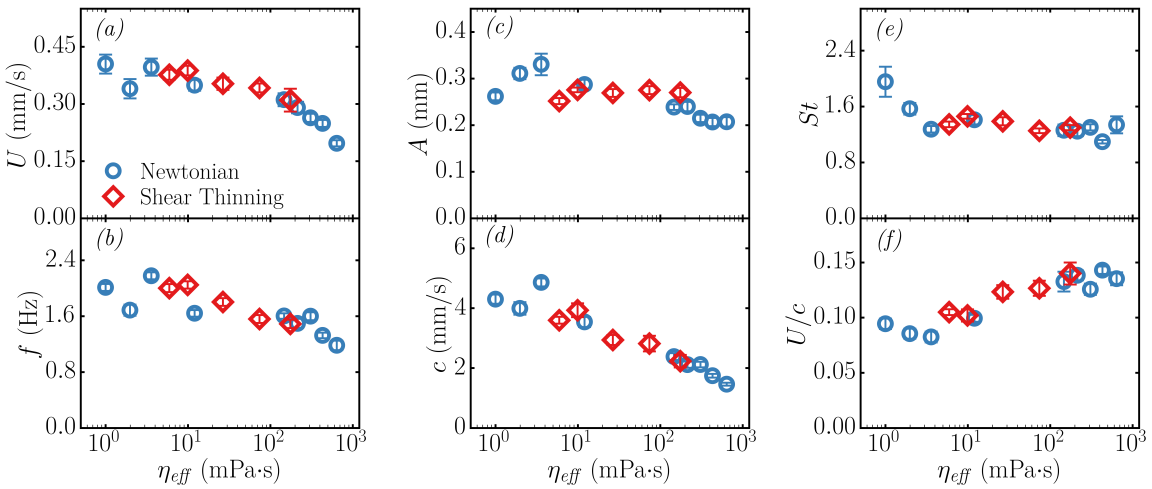

Figure 7: Summary of nematode kinematics for Newtonian (○) and shear-thinning (◇) fluids. *(a)* Swimming speed U, *(b)* frequency f, *(c)* head amplitude A, *(d)* wave speed c, *(e)* Strouhal number St and *(f)* kinematic efficiency U/c as a function of effective viscosity η_{eff}. Each data point represents the mean and standard error of approximately 15 recordings.

the aforementioned theoretical study. For example, the nematode is of finite-length and swims using large-amplitude waves that decay from head to tail, while the theoretical work focuses on an infinite, two-dimensional waving sheet of prescribed, small-amplitude kinematics. Thus, quantitative agreement is not expected.

We can also compare our findings to numerical simulations (Montenegro-Johnson et al., 2012, 2013) that have predicted an enhancement in swimming speed; however, the enhancement predicted by this study is for a swimmer with an elliptical head and a linearly increasing amplitude from head to tail; since *C. elegans* has no "head" and conversely has a decreasing amplitude from head to tail, these differences in geometry and stroke may explain the discrepancy between these simulations' predictions and our experimental measurements (Montenegro-Johnson et al., 2012, 2013).

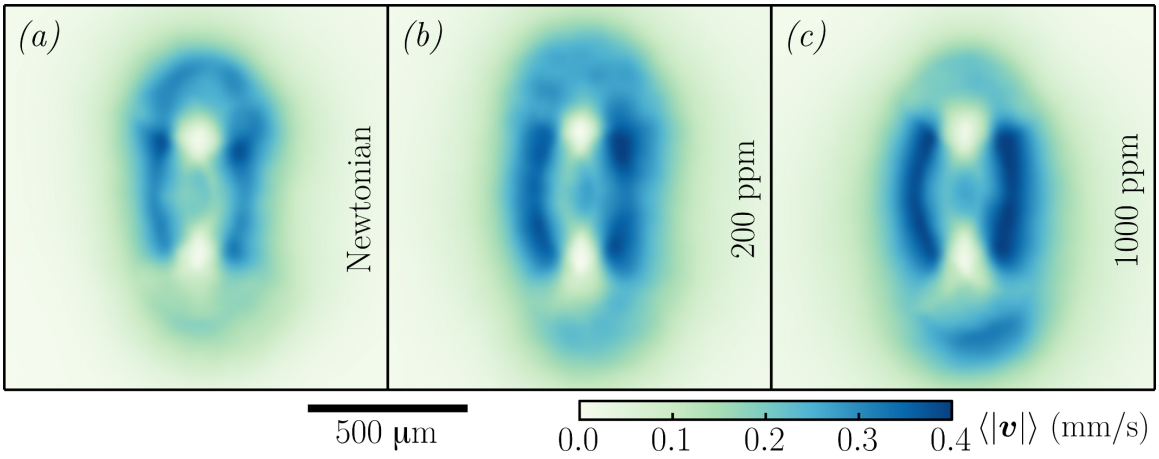

Figure 8: *(a-c)* Time-averaged fluid velocity magnitude for one beating cycle of *C. elegans* in *(a)* Newtonian buffer solution, *(b)* shear-thinning 200 ppm XG solution, and *(c)* shear-thinning 1000 ppm XG solution.

3.3. Velocimetry, Flow Fields, and Streamlines

In the preceding section, we showed that the swimming strokes of nematodes in shear-thinning and Newtonian fluids are quite similar (if not identical). However, the same kinematics may generate different velocity fields. Since the swimming stroke corresponds to the imposed fluid boundary conditions, in Newtonian fluids we expect flow fields to have a common morphology, with velocity magnitudes merely scaling with viscosity. However, under the same boundary conditions, a non-Newtonian constitutive relation might result in measurable changes to the flow fields. To investigate this possibility, we use particle tracking to measure the flow fields around swimming *C. elegans* in shear-thinning and Newtonian fluids. We seed the fluids with 3.1 μm-diameter fluorescent polystyrene spheres, which are tracked in space and time (Sznitman et al., 2010b; Gagnon et al., 2013). The particles are very dilute ($< 0.5\%$ by volume) and do not alter the fluid rheology.

Because the nematode's swimming gait is periodic (Fig 1*(c)*), we can significantly increase the spatial resolution of our flow field measurements by using a phase averaging scheme. We condense multiple beating cycles into a single "master" cycle by matching frames with

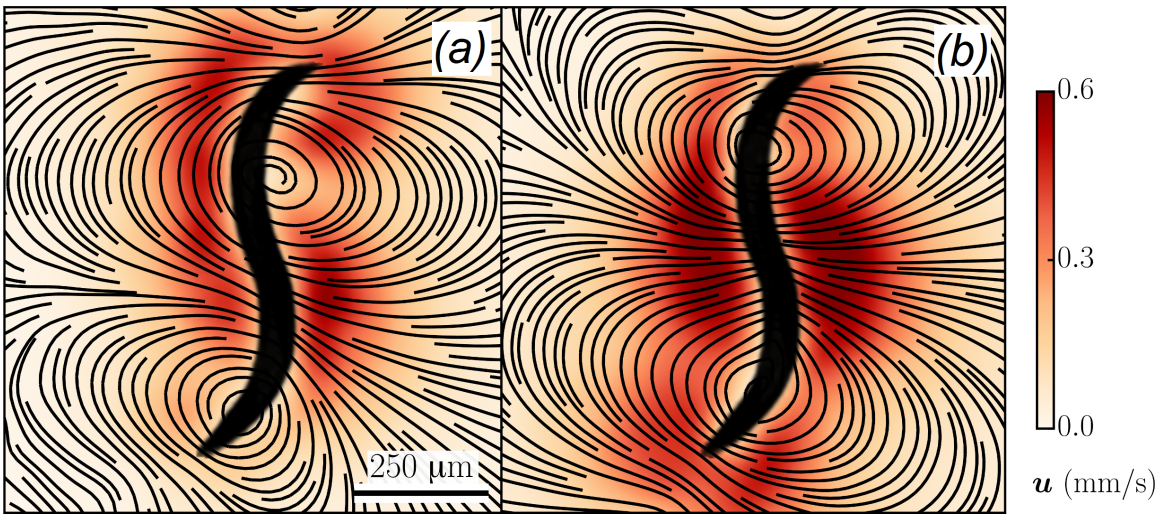

Figure 9: *(a)* Snapshot of the streamlines obtained using particle tracking techniques around *C. elegans* in a Newtonian buffer solution ($\eta = 1$ mPa·s) at the moment of maximum fluid velocity. Color represents the magnitude of the local velocity field. (b) Snapshot of the streamlines around *C. elegans* during the same phase of motion in a strongly shear-thinning fluid (Carreau timescale $\lambda_{Cr} \approx 6.5$ and power-law index $n \approx 0.5$). See Fig. 6 for more detail.

the same curvature profile $\kappa(s,t)$, using a least-squares algorithm. This master cycle comprises body shapes and velocity fields at approximately 65 different phases. For more details on this technique, see Sznitman et al. (2010b).

Figure 8 shows time-averaged velocity magnitude fields in *(a)* buffer solution (Newtonian), *(b)* 200 ppm XG solution, and *(c)* 1000 ppm XG solution over one beating cycle. Two features are immediately obvious. First, the regions of high velocity (dark color) at the nematode's midsection seem to change and intensify as XG concentration and shear-thinning effects are increased. Second, there is an overall decrease in average velocity near the head and an increase near the tail as XG concentration increases. These data show that velocity fields generated by swimming nematodes can be modified by shaer-thinning effects, even as the imposed swimming kinematics remain unchanged.

To better examine shear-thinning effects on the velocity fields, we focus on one particular phase of the beating cycle. While we expect shear-thinning effects at every phase, we

examine the phase with the largest average shear rate, since this snapshot should reveal the most pronounced differences between Newtonian and shear-thinning fluids. Figure 9 shows the fluid streamlines and velocity magnitude (color) at one phase in *(a)* M9 buffer solution and *(b)* 1000 ppm XG solution. The streamlines suggest that in the shear-thinning case, the characteristic "head" and "tail" vortices have shifted towards the head and appear more concentrated. The difference in velocity magnitudes near the midsection is located near the center of the head vortex, suggesting a potential way to quantify shear-thinning effects.

3.4. Quantifying the Role of Shear-Thinning through Vorticity

So far we have shown that shear-thinning viscosity has negligible effect on the nematode's swimming kinematics (figure 7) but it does seem to affect the velocity fields generated by swimming (figure 9). Here, we quantify those effects and seek to connect them with the fluids' shear-thinning rheology. We begin by inspecting the flow structure (vortex) near the nematode's head for both the Newtonian and shear-thinning fluids (figure 9*(a)* and *(b)*). For each fluid, we take the velocity field at the same phase as in figure 9, sampled at a grid of points spaced 21 μm apart. We compute vorticity $\boldsymbol{w}$ in two dimensions, so that $w_z \equiv \partial v_y/\partial x - \partial v_x/\partial y$.

Figures 10*(a)* and *(b)* show vorticity fields for the 50 and 500 ppm XG solutions, respectively, with the head vortices outlined; note that the 50 ppm XG vorticity map is not substantially different from the Newtonian case (not shown). We define the head vortex as the region near the head with $|\boldsymbol{w}|$ greater than 10% of the local maximum. The head vortex is in fact the region of highest vorticity over the entire flow field. The two vorticity fields suggest that increasing the concentration of XG, and thus the shear-thinning behavior of the fluid, increases the magnitude and size of the head vortex. We note that this is not simply due to a change in bulk or "average" viscosity, since increasing viscosity would merely scale the vorticity field without changing its shape.

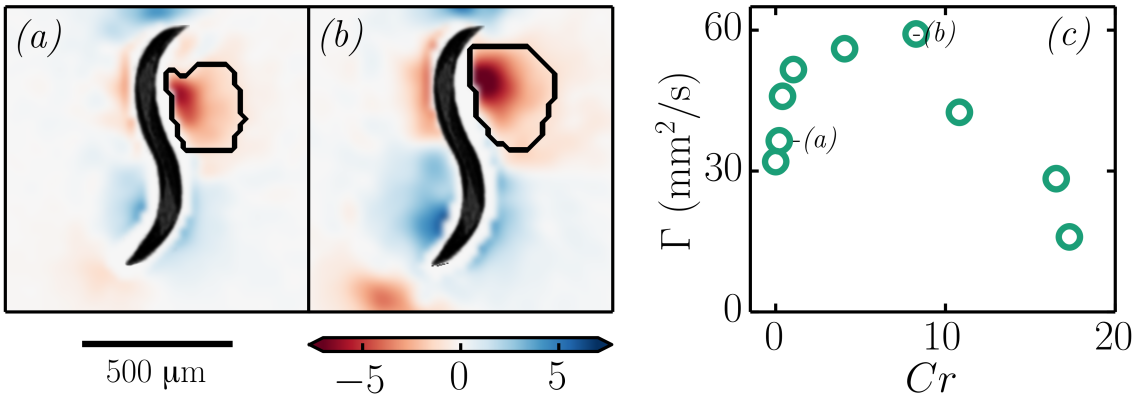

Figure 10: Vorticity map calculated for *C. elegans* swimming in *(a)* 50 ppm XG in M9 and *(b)* 500 ppm XG in M9. The region of the head vortex (outlined in black) is defined as the region with vorticity greater than 10% of the local maximum. *(c)* Circulation Γ of the head vortex for M9 and shear-thinning fluids as a function of the expected local importance of shear thinning, $Cr = \lambda_{Cr}\overline{\dot{\gamma}}$, where λ_{Cr} is the Carreau timescale and $\overline{\dot{\gamma}}$ is the measured average local shear rate.

Next, we measure the circulation or vorticity flux Γ, which can be thought of as the total vorticity normal to the surface of interest. We compute Γ as the discrete integral of vorticity $w_{z,i}$ at each grid cell i within the vortex region: $\Gamma = \sum a w_{z,i}$, where a is the area of a grid cell. We also use the velocity field and fluid rheology to estimate the *expected* importance of shear-thinning behavior in the vortex region. This is quantified with a Carreau number $Cr = \lambda_{Cr}\overline{\dot{\gamma}}$. The characteristic vortex shear rate $\overline{\dot{\gamma}}$ is the root-mean-squared average over all grid cells in the vortex, where each cell's local shear rate is computed as $\dot{\gamma} \equiv \partial v_x/\partial y + \partial v_y/\partial x$.

Figure 10*(c)* summarizes our measurements of circulation Γ for a range of Carreau numbers Cr, corresponding to a Newtonian fluid (M9, $Cr = 0$) and all tested XG concentrations. We find that circulation is generally enhanced as shear-thinning effects are increased. We also observe a similar trend in vorticity magnitude both temporally and spatially for the entire cycle. At high Cr (corresponding to high XG concentrations), the increase in overall viscosity appears to suppress circulation: these data points are close to the power-limited

regime, and for fluids above $Cr \approx 15$, the shear stresses needed to access the shear-thinning regime exceed $\sigma = 0.1$ Pa. However, for $0 < Cr < 15$ (XG concentrations ≤ 1000 ppm), the measured circulation and vorticity are larger than in the Newtonian case, and this suggests agreement with previous theoretical work, which predicted enhanced vorticity in shear-thinning fluids (Vélez-Cordero and Lauga, 2013).

3.5. The cost of swimming in shear-thinning fluids

We now begin our discussion on estimating the cost of swimming or mechanical power of swimming *C. elegans* from velocimetry and nematode tracking data. Here, we consider the flow of an incompressible fluid at low Reynolds number. Under these conditions, the equation of motion and the continuity equation are:

$$\boldsymbol{\nabla} \cdot \boldsymbol{\sigma} = -\boldsymbol{\nabla} p + \boldsymbol{\nabla} \cdot \boldsymbol{\tau} = 0 \tag{3.2}$$

$$\boldsymbol{\nabla} \cdot \boldsymbol{u} = 0, \tag{3.3}$$

where $\boldsymbol{u}$ is the fluid velocity and $\boldsymbol{\sigma}$ is the total stress tensor. The stress is defined as

$$\boldsymbol{\sigma} = -p\boldsymbol{I} + \boldsymbol{\tau}, \tag{3.4}$$

where p is pressure, $\boldsymbol{I}$ is the identity tensor, and $\boldsymbol{\tau}$ is the shear (deviatoric) stress. Steady flow is assumed since the "frequency" Reynolds number is much less than one: $Re_f = \rho A^2 f / \mu \ll 1$, where f and A are the nematode's beating frequency and amplitude, respectively (Childress, 1981).

Next, we consider the energy expenditure of a swimming nematode under the above conditions and assumptions. Conservation of energy requires the power expended by the swimming nematode by deforming its body to be equal to the energy dissipation rate of the surrounding fluid. This relationship naturally provides two methods for estimating the

cost of swimming or mechanical power as we will see below. We define the mechanical power associated with the motion of the nematode surface S as its rate of work:

$$P = -\int_S \boldsymbol{n} \cdot \boldsymbol{\sigma} \cdot \boldsymbol{u} \, \mathrm{d}S, \tag{3.5}$$

where $\boldsymbol{u}$ is the velocity of the surface. We assume that inertial and body forces are negligible for a swimming nematode, and the only forces acting on the swimmer are viscous surface forces $\boldsymbol{F} = \int_S \boldsymbol{n} \cdot \boldsymbol{\sigma} \, \mathrm{d}S = 0$. This integral of the surface force must be zero since the swimmer is self-propelled and force-free (Lauga and Powers, 2009).

Next, we can apply the divergence theorem to Eq. 3.5 to transform the surface integral into a volume integral over the surrounding fluid V with the assumption that $\boldsymbol{u}$ vanishes far from the swimmer (Lighthill, 1976). This transforms the surface's rate of work into the rate of viscous dissipation of the fluid:

$$P = -\int_S \boldsymbol{n} \cdot \boldsymbol{\sigma} \cdot \boldsymbol{u} \, \mathrm{d}S = \int_V \boldsymbol{\nabla} \cdot (\boldsymbol{\sigma} \cdot \boldsymbol{u}) \, \mathrm{d}V. \tag{3.6}$$

Distributing the divergence operator on the volume integral yields:

$$P = -\int_S \boldsymbol{n} \cdot \boldsymbol{\sigma} \cdot \boldsymbol{u} \, \mathrm{d}S = \int_V (\boldsymbol{\nabla} \cdot \boldsymbol{\sigma}) \cdot \boldsymbol{u} + \boldsymbol{\sigma} : \boldsymbol{\nabla} \boldsymbol{u} \, \mathrm{d}V. \tag{3.7}$$

By Stokes equation (Eq. 3.2), the first term in the volume integral must be zero. Furthermore, we can substitute $\boldsymbol{\sigma}$ in the volume integral with the definition of the stress tensor $\boldsymbol{\sigma}$ (Eq. 3.4) so that:

$$P = -\int_S \boldsymbol{n} \cdot \boldsymbol{\sigma} \cdot \boldsymbol{u} \, \mathrm{d}S = \int_V -p\boldsymbol{I} : \boldsymbol{\nabla} \boldsymbol{u} + \boldsymbol{\tau} : \boldsymbol{\nabla} \boldsymbol{u} \, \mathrm{d}V. \tag{3.8}$$

Note that $\boldsymbol{I} : \boldsymbol{\nabla u} = \boldsymbol{\nabla} \cdot \boldsymbol{u} = 0$, for an incompressible fluid, yielding the energy balance:

$$P = -\int_S \boldsymbol{n} \cdot \boldsymbol{\sigma} \cdot \boldsymbol{u} \, \mathrm{d}S = \int_V \boldsymbol{\tau} : \boldsymbol{\nabla u} \, \mathrm{d}V. \tag{3.9}$$

Lastly, the right-hand side of Eq. 3.9 is equal to the fluid's viscous dissipation:

$$\Phi = \int_V \boldsymbol{\tau} : \boldsymbol{\nabla u} \, \mathrm{d}V. \tag{3.10}$$

Equation 3.9 reveals two methods for estimating the cost of swimming via both a calculation of the swimmer's mechanical power (P, Eq. 3.5) and an estimate of the surrounding fluid's viscous dissipation rate (Φ, Eq. 3.10). In what follows, we will use Equation 3.9 along with experimental data (nematode tracking, velocimetry, and rheology) to estimate the cost of swimming for *C. elegans*. There are three necessary ingredients: *(i)* the instantaneous position of the surface S (obtained from nematode tracking) and the corresponding fluid volume V, *(ii)* a spatially differentiable flow field $\boldsymbol{u}$ (from particle tracking), and *(iii)* a constitutive model for the fluid stresses $\boldsymbol{\sigma}$ (from rheology and Equation 3.1). First, we measure the instantaneous position of the surface S and its outward normal $\boldsymbol{n}$ by tracking the body of the nematode using bright-field microscopy (Fig. 1*(a)*). Image processing provides an outline of the nematode's body in a two-dimensional plane; to estimate S, we multiply the observed body shapes by the diameter of the nematode's body (80 µm) to form a thin surface area. For our estimate of the viscous dissipation rate, we consider the area formed by the plane of observation in our region of interest (approximately 2 mm by 2 mm). Beyond this region of interest, the velocities of the fluid are below the noise level of our particle tracking measurements. Similar to our surface integral, we multiply this area by the diameter of the nematode's body (80 µm) to form a small, thin volume. For both integrals (surface and volume), we note this assumes a uniform planar flow field within 40 µm of the mid-plane of the worm. The thinness of the selected volume aims to

minimize errors associated with the three-dimensional nature of the flow. Second, using particle tracking velocimetry, we measure the velocity fields $\boldsymbol{u}$ and, because $\boldsymbol{u}$ is spatially resolved, the associated shear rate tensor $\dot{\boldsymbol{\gamma}}$ (Fig. 9*(a)* and *(b)*).

Lastly, we consider the constitutive equation necessary to estimate the fluid stress tensor $\boldsymbol{\sigma} = -p\boldsymbol{I} + \boldsymbol{\tau}$. The pressure p is found by integrating Stokes equation from the boundary of our velocity field to the fluid-swimmer interface; note that the contribution of the isotropic static pressure p_0 vanishes over a closed integral and as a result is negligible. For Newtonian fluids, we simply use Newton's law of viscosity $\boldsymbol{\tau} = \eta\dot{\boldsymbol{\gamma}}$. For shear-thinning fluids, the shear (deviatoric) stress is estimated for each beating phase by first differentiating the velocity field to obtain a shear rate field. We then use the Carreau-Yasuda model (Eq. 3.1) along with the rheological data shown in Fig. 6*(b,c)* to calculate a viscosity field for all shear-thinning fluids.

Figure 11 shows snapshots of the spatial viscosity fields normalized by zero-shear viscosity η/η_0 for a particular beating phase in different XG solutions. Viscosity is color-coded such that blue corresponds to zero-shear viscosity and yellow highlights regions of strong shear-thinning behavior; one can also consider locations with decreased viscosity as highlighting regions of large shear rate magnitude in the flow. Figure 11*(a)* shows the estimated viscosity field for the 200 ppm XG solution, which has a power-law index of $n = 0.85$ and a Carreau timescale of $\lambda_{Cr} = 0.4$ s. The largest decrease in normalized viscosity for this fluid is approximately 15%. Figure 11*(b)* shows the result for a solution of $n = 0.70$ and $\lambda_{Cr} = 1.2$ s, which exhibits a decrease in viscosity of nearly 30%. Finally, Fig. 11*(c)* shows the viscosity fields for nematode's swimming in a XG solution of $n = 0.60$ and $\lambda_{Cr} = 3.5$ s. Here, we observe the formation of a highly-thinned fluid envelope around the nematode that extends approximately 0.5 mm (or half body length) away from the nematode's body; the viscosity decrease near the swimmer is approximately 60%. The viscosity fields for nematodes swimming in highly shear-thinning fluids, $n < 0.5$ and $\lambda_{Cr} > 5$ (not shown),

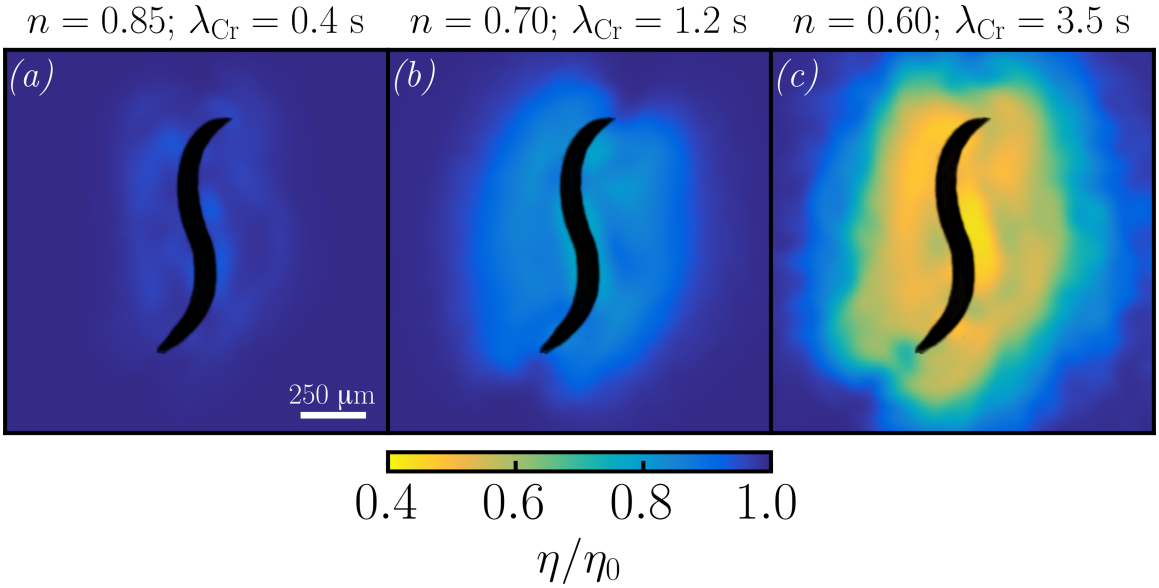

Figure 11: Viscosity fields, normalized by the fluid's zero-shear viscosity η_0, for a selection of XG solutions at an instant in time: *(a)* 200 ppm, *(b)* 300 ppm, *(c)* 500 ppm XG.

show similar behavior to Fig. 11*(c)*, and the normalized viscosity can decrease by more than an order of magnitude (from 1 to 0.1).

Measurements of the surface S, differentiable velocity fields $\boldsymbol{u}$, and the stress $\boldsymbol{\sigma}$ allow us to investigate whether a local decrease in viscosity modifies the cost of swimming. We compute both the mechanical power of the swimmer (P, Eq. 3.5) and the rate of viscous dissipation in the fluid (Φ, Eq. 3.10). This allows for a interesting comparison between different methods of computing the mechanical power of swimming organisms at low *Re* from experimental data. We note that particle tracking techniques can only resolve velocity fields and shear rates 40 μm from the boundary of the swimmer. Our calculation of drag force and power (Eq. 3.5) are therefore somewhat hindered by our ability to make measurements close to the swimmer. We then compare our estimations of power from experimental data to recent theoretical (Vélez-Cordero and Lauga, 2013) and numerical results (Li and Ardekani, 2015).

Results for both mechanical power and viscous dissipation rate are shown in Fig. 12.

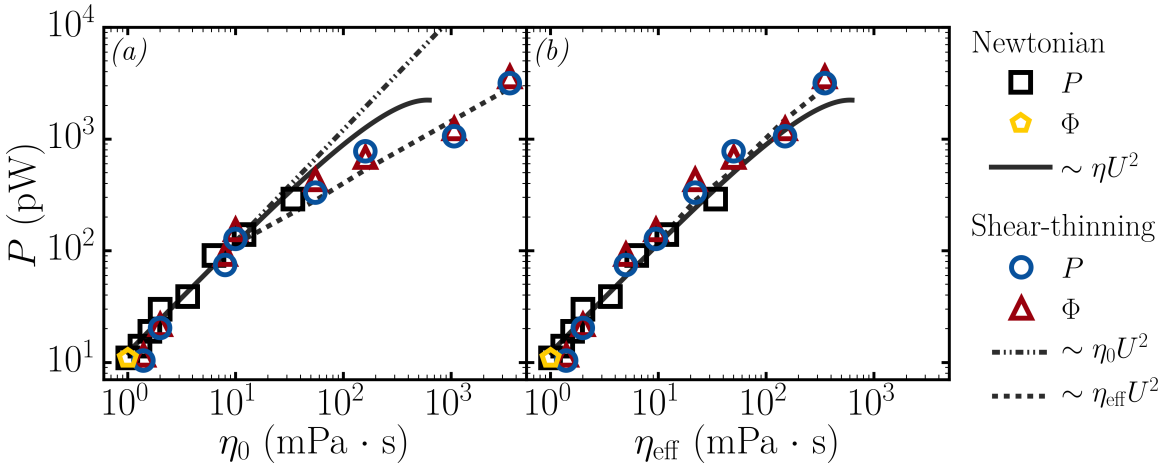

Figure 12: *(a)* Cost of swimming as a function of zero-shear viscosity η_0 using each side of Eq. 3.9. For Newtonian fluids: mechanical power (□, from Sznitman et al. (2010b)), viscous dissipation rate (⬠, buffer only), and the scaling $P \sim \eta U^2$ (solid line) calculated from our kinematics data (Gagnon et al., 2014a). For shear-thinning fluids: mechanical power (○), viscous dissipation rate (△), and the scalings $P \sim \eta_0 U^2$ (dash-dot line) and $P \sim \eta_{\text{eff}} U^2$ (dashed line). *(b)* Mechanical power and viscous dissipation rate replotted versus effective viscosity η_{eff}.

The calculation of mechanical power P (Eq. 3.5) as a function of zero-shear-viscosity η_0 is shown for several shear-thinning fluids (○) and Newtonian solutions (□). Also shown is the viscous dissipation rate Φ (Eq. 3.10) for the same shear-thinning fluids (△) as well as a Newtonian buffer solution (⬠). Results from the measurement of mechanical power and viscous dissipation rate show quite reasonable agreement, and suggest that both methods can be used to estimate the cost of swimming of low-*Re* organisms.

The data presented in Fig. 12*(a)* show that the estimated mechanical power increases linearly with fluids viscosity for *C. elegans* swimming in Newtonian fluids. A deviation from this linear behavior is found for high viscosity fluids because the nematode is power-limited (Shen and Arratia, 2011); this deviation starts for fluid viscosities greater than approximately 30 mPa·s. For nematodes swimming in Newtonian fluids, we expect the mechanical power to scale as $P \sim \eta U^2$, where U is the swimming speed of the nematode; the black line shows this scaling using our previously obtained experimentally-measured

kinematics (in Newtonian fluids) to provide values of U for a range of fluid viscosities (Shen and Arratia, 2011; Gagnon et al., 2014a). This scaling indicates that power should increase linearly with viscosity and indeed the calculation of mechanical power in Newtonian fluids supports this linearity. This indicates that the nematode's kinematics (i.e. swimming speed) are largely insensitive to changes in viscosity for $\eta < 30$ Pa·s (Sznitman et al., 2010b). For larger values of η, however, our data show a deviation from a linear scaling for $P \sim \eta U^2$ because the nematode is power-limited.

For shear-thinning fluids, the mechanical power at low viscosity also increases linearly with increasing zero-shear viscosity. At moderate to large viscosities ($\gtrsim$ 30 mPa·s), mechanical power increases sub-linearly with zero-shear viscosity (η_0). In order to interpret these data, Fig. 12*(a)* also shows two scalings for shear-thinning fluids generated from our experimentally-measured kinematics in shear-thinning fluids. The first scaling ($P \sim \eta_0 U^2$), shown as a dash-dot line. This curve is essentially a continuation of the linear scaling observed at low viscosities in Newtonian fluids. The second scaling ($P \sim \eta_{\text{eff}} U^2$), shown as a dashed line, appears to captures the sub-linearity of our mechanical power calculations; the value of η_{eff} is defined as the average viscosity over the range of characteristic shear rates produced by the organism (Gagnon et al., 2014a). Figure 12*(b)* evaluates the robustness of this scaling; here, the mechanical power and viscous dissipation measurements are shown versus effective viscosity (η_{eff}) and compared with the Newtonian scaling $P \sim \eta U^2$, which remains unchanged. The data collapses onto the Newtonian scaling, suggesting that an organism's cost of swimming in a generalized Newtonian fluid is reasonably well-predicted by estimating a fluid's effective viscosity for a given swimming gait. This confirms a previous hypothesis made from the kinematics of *C. elegans* as a function of effective viscosity (Gagnon et al., 2014a; Gagnon and Arratia, 2016).

Previous work on undulatory swimming in shear-thinning fluids, however, generally compares mechanical power to the equivalent Newtonian power, defined as $P_N = P(\eta_0)$,

and broadly predicts that shear-thinning viscosity decreases the cost of swimming (Vélez-Cordero and Lauga, 2013; Li and Ardekani, 2015). Since a shear-thinning fluid's effective viscosity must always be less than or equal to its zero-shear viscosity, our findings in Fig. 12*(a)* suggest agreement. However, these theoretical (Vélez-Cordero and Lauga, 2013) and numerical (Li and Ardekani, 2015) studies also suggest theoretical scalings using the Carreau-Yasuda model (Eq. 3.1) for mechanical power relative to the Newtonian case P/P_N. While the work of Vélez-Cordero and Lauga (2013) uses a small-amplitude approximation and diverges at high Carreau number Cr_k, Li and Ardekani (2015) have recently extended this scaling to large amplitudes:

$$P/P_N = 1 - (1 - \eta_\infty/\eta_0)\left(1 - \left(1 + Cr_k^2\right)^{(n-1)/2}\right). \tag{3.11}$$

We note that Li and Ardekani (2015) multiply the square of the kinematic Carreau number Cr_k by the constant $3/8$, such that the first term of the Taylor expansion of Eq. 3.11 matches the theoretical power of small amplitude undulatory sheet in a generalized Newtonian fluid (Vélez-Cordero and Lauga, 2013; Li and Ardekani, 2015). Since we are not performing an expansion of this equation and are instead inserting experimentally-measured swimming kinematics and fluid rheology, we take this constant to be one in our experimental system.

This theoretical scaling for relative power (Eq. 3.10) now gives us a method for making a quantitative comparison between the proposed scaling and the methods for estimating mechanical power from Eq. 3.9. By using our rheology data (Fig. 6) and kinematics data (Gagnon et al., 2014a), we can estimate η_∞/η_0 and directly compute Cr_k to obtain an approximation of normalized power P/P_N. We show this experimental estimate of P/P_N as a function of Cr_k in Fig. 13 alongside our measurements of mechanical power using both methods discussed above, *(i)* mechanical power (P, ○) and *(ii)* viscous dissipation rate (Φ, △). We note that we do not observe a strongly power-limited regime for *C. elegans* swim-

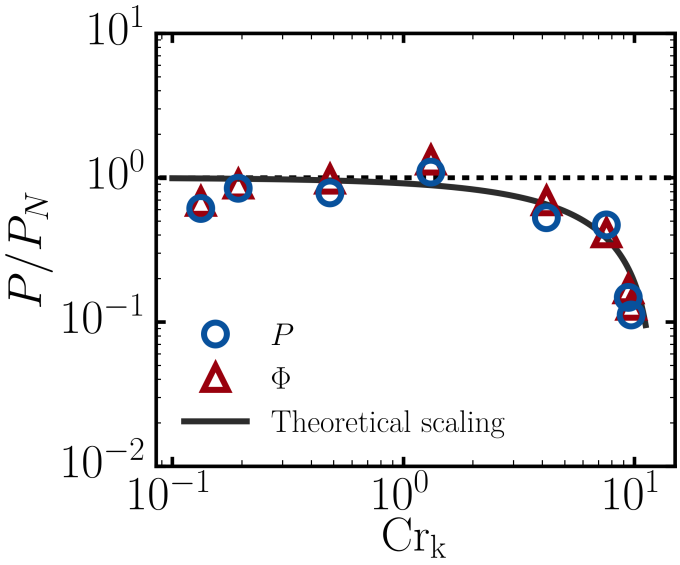

Figure 13: Normalized mechanical power (○) and viscous dissipation rate (△) as a function of Cr_k; the dashed line represents the Newtonian case. The transition from $P/P_N \approx 1$ to $P/P_N < 1$ occurs at $Cr_k = \mathcal{O}(1)$. The solid black line is the theoretical scaling generated from our rheology and kinematics data, given by Eq. (3.11) (Li and Ardekani, 2015).

ming in shear-thinning fluids, though we observe some deviations from a linear scaling for Newtonian fluids; it is in such regime that one would expect significant deviations from the theoretical calculations, which assume the swimmer to have infinite power.

We find good agreement among between our calculations and the theoretical scaling based on our kinematics and rheology data: at $Cr_k \sim \mathcal{O}(1)$, the cost of swimming in shear-thinning fluids transitions from $P/P_N \approx 1$ to $P/P_N < 1$. Indeed, we now gain considerable confidence in predicting the cost of swimming using only rheology (η_0, η_∞, and λ_{Cr}) and simple kinematics (A, f, and k).

It follows that we can hypothesize the cost of transport for an undulatory swimmer in a generalized Newtonian fluid. For example, in a shear-thickening fluid with the same constitutive model (Eq. 3.1) but now with a power law index $n > 1$ and $\eta_0 < \eta_\infty$, we predict that a nematode would require more power compared to a Newtonian fluid of the same zero-shear viscosity. Additionally, when scaled by effective viscosity, we expect

the cost of swimming in a shear-thickening fluid to collapse onto the Newtonian scaling, similar to our shear-thinning data in Fig. 12*(b)*.

CHAPTER 4 : Swimming in concentrated, structured fluids

Many fluids of practical interest contain solids and/or polymers which form structures at an intermediate scale between the size of a molecule and the macroscopic length scale of the system (Larson, 1999). Such "complex fluids" often display non-Newtonian rheological behavior including shear-thinning viscosity and viscoelasticity. The interplay between the fluid's internal structure (e.g. polymer networks) and self-propulsion is critical to many biological processes such as reproduction (Guzick et al., 2001), bacterial infection (Josenhans and Suerbaum, 2002), and bio-degradation in soil (Alexander, 1991). For example, the bacteria *H. pylori* can modulate the acidity of gastric mucus and thus untangle glycoprotein networks, reducing the resistance of mucus (Celli et al., 2009), and nematodes can burrow through the networks present in wet soil aiding in soil aeration, water storage, and soil fertility (Juarez et al., 2010; Jung, 2010). Understanding swimming in complex fluidic environments is thus pertinent to the treatment of human diseases as well as the characterization and maintenance of ecological systems.

Experimental observations have revealed that polymer networks can enhance the swimming speed of flagellated bacteria moving in solutions containing long-chain polymer molecules (Berg and Turner, 1979; Schneider and Doetsch, 1974). For these small organisms ($L < 10$ μm), it has been argued that the main mechanism for this propulsion enhancement is due to the benefits of pushing against a quasi-rigid polymer network (Berg and Turner, 1979; Magariyama and Kudo, 2002). The role of the mechanical properties of fluid internal networks on an organism's swimming behavior has also been investigated in numerical (Fu et al., 2010; Du et al., 2012; Magariyama and Kudo, 2002; Nakamura et al., 2006) and theoretical (Leshansky, 2009) studies. Numerical studies of swimming in fluids structured with polymer networks resembling natural environments have postulated that the shapes and dynamics of internal networks are accounted for by two effective anisotropic viscosities (Magariyama and Kudo, 2002; Nakamura et al., 2006), which qual-

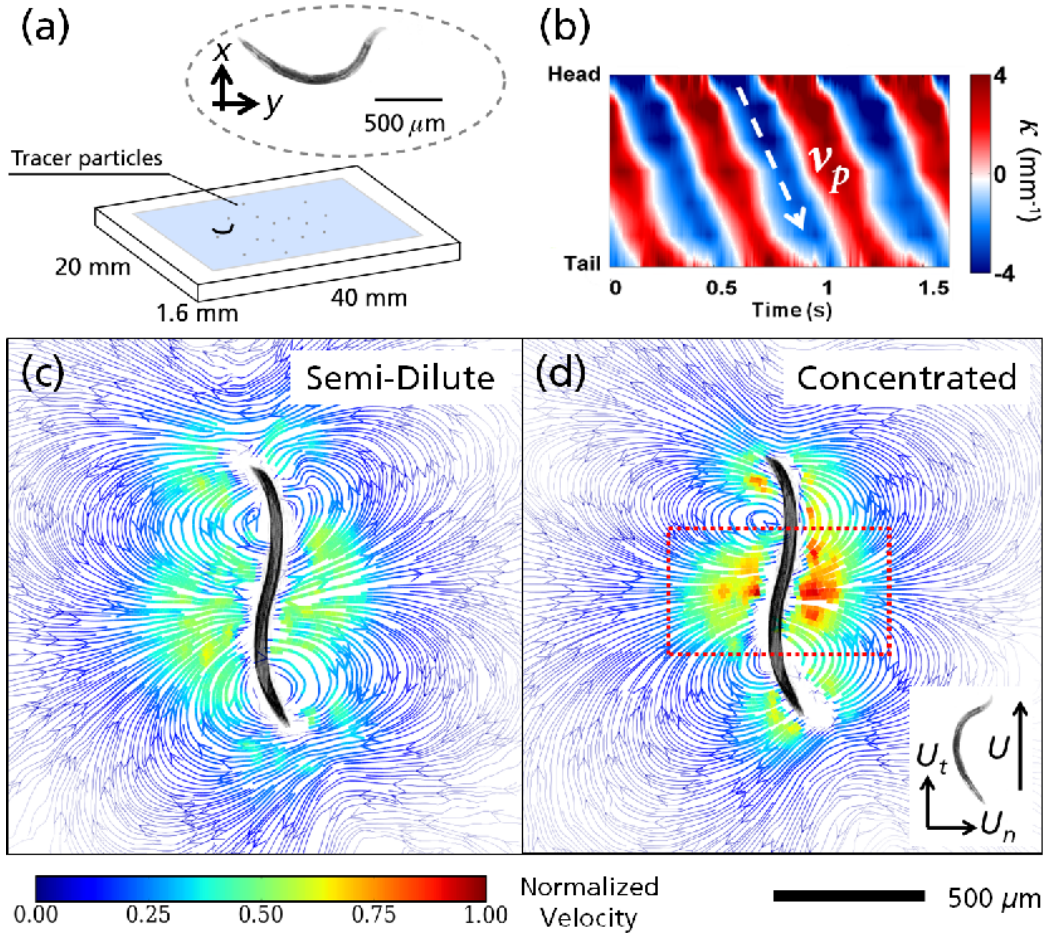

Figure 14: *(a)* Schematic of nematode *C. elegans* swimming in a sealed fluidic chamber. *(b)* Nematode's centerline and body curvature during swimming. Curvature plot for approximately 3 beating cycles reveals traveling wave propagating from head to tail. Wave speed illustrated by the white dashed line with arrow indicating the direction. *(c, d)* Flow streamlines color-coded by normalized velocity magnitude during swimming for 2000 ppm (semi-dilute) and 4000 ppm (concentrated) cases. The red box highlights a region of high relative flow in the concentrated regimes; inset defines normal and tangential components relative to the worm body.

itatively explain some of the observed propulsion enhancement (Berg and Turner, 1979; Schneider and Doetsch, 1974). Such anisotropic viscosities, however, are difficult to measure and apply to quantitative analysis. In heterogeneous, gel-like environments, modeled by embedding stationary objects in an incompressible viscous fluid, the swimming speed of a microorganism can be enhanced by the underlying structures in the fluid (Leshansky, 2009). For internal networks made of small molecules, such as a binary blend of two intermixed fluids, a two-fluid model predicts an enhancement in swimming speed for stiff and compressible networks (Fu et al., 2010), and a reduction in swimming speed when local distributions of volume fractions of the two phases scale differently for thrust and drag (Du et al., 2012). Overall, the observed propulsion speed variations in these studies underscore the important role of the fluid structures on the swimming behavior of microorganisms.

In this manuscript, we investigate the effects of polymer networks on the swimming dynamics of the nematode *Caenorhabditis elegans* in experiments using tracking and velocimetry methods. Polymer networks are formed by controlling the concentration of the biocompatible rod-like polymer xanthan gum in water. We find an enhancement of approximately 65% in the nematode's swimming speed in concentrated polymeric solutions compared to semi-dilute solutions. Due to the relatively large size of the nematode ($L \approx 1$ mm) compared to the polymer networks (~ 10 μm), the mechanism of pushing against a quasi-static polymer network is insufficient to explain the increase in swimming speed. We argue that the propulsion enhancement arises from local shear-induced anisotropy.

4.1. Experimental Methods

Experiments are performed in an acrylic fluidic chamber (Fig. 14*(a)*) that is 20 mm wide, 40 mm long and 1.6 mm deep. All experiments are performed with wild-type, adult *C. elegans* that are on the average 1 mm in length and 80 μm in diameter. The nematodes

swimming motion is imaged using a microscope with a depth of field of 30 μm and a fast camera operated at 100 frames per seconds in order to accurately resolve small body displacements. To minimize boundary effects from the top and bottom walls, the imaging plane is focused at the center of the chamber. All data presented here pertain to nematodes swimming at the center plane of the fluidic channel. Out-of-plane recordings are discarded. An average of 15 nematodes are recorded for each experiment.

Figure 14*(a)* shows a sample snapshot of a nematode swimming in the water-like buffer solution M9. Here, swimming speed U is calculated by differentiating the nematode's centroid position over time; we find $U \approx 0.35$ mm/s for nematodes swimming in M9 solutions. The nematode's Reynolds number $Re = \rho UL/\mu \approx 0.2$, where L is the nematode's length (1 mm), ρ is fluid density, and μ is the fluid viscosity (1 mPa·s). The nematode's shape-line in each frame is extracted by in-house software (Krajacic et al., 2012) to calculate the nematode's body curvature, defined as $\kappa = d\phi/ds$. Here, ϕ is the angle made by the tangent to the x-axis in the laboratory frame at each point along the body centerline, and s is the arc length coordinate from the head of the nematode ($s = 0$) to its tail ($s = L$). Fig. 14*(b)* shows the spatio-temporal evolution of the nematode's body curvature $\kappa(s, t)$ for approximately three swimming cycles. This curvature plot shows the existence of periodic, well-defined, and diagonally oriented lines characteristic of bending waves propagating in time along the nematode body length, from which important kinematic quantities such as beating frequency f and wave-speed ν_p are obtained (Sznitman et al., 2010b); wave-speed is illustrated using a white dashed line with an arrow indicating the direction of waves in Fig. 14*(b)*. We find that $f \approx 2$ Hz and $\nu_p = 5$ mm/s for nematodes swimming in M9 buffer solution.

Polymeric fluids are prepared by adding small amounts of xanthan gum (XG) to deionized water. Xanthan gum is a semi-rigid rod-like polymer with a molecular weight of 2×10^6 Da (Sigma Aldrich, G1253). Polymer concentration ranges from 300 ppm to 5000 ppm by

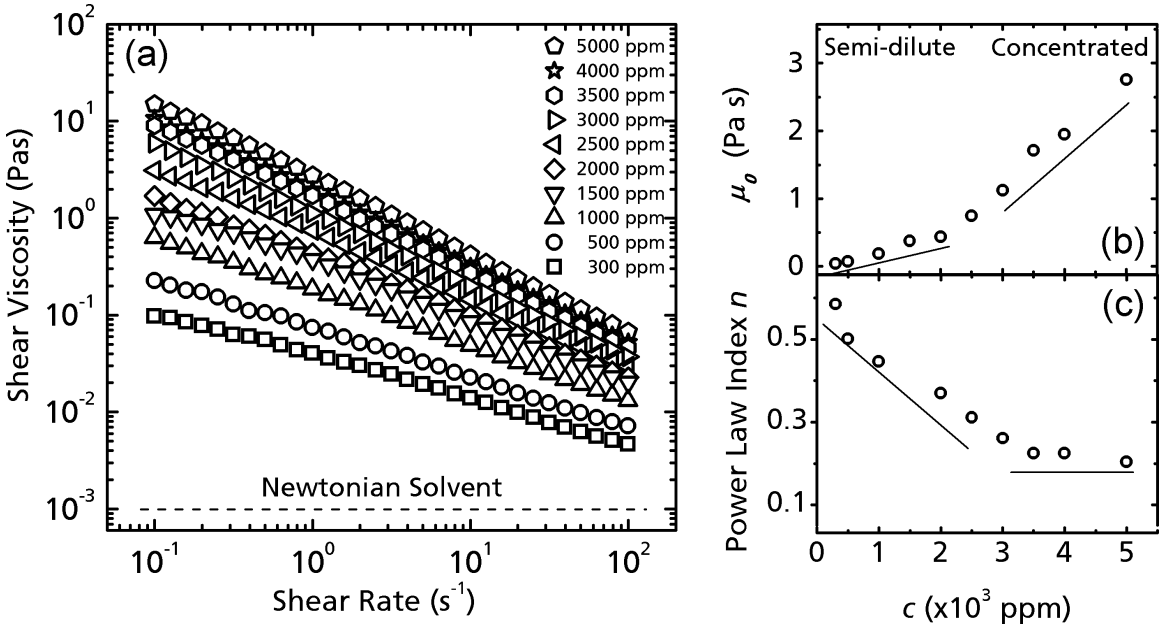

Figure 15: *(a)* Shear viscosity of xanthan gum solutions showing power law behavior. *(b)* Stress relaxation data for XG solutions fit to a linear viscoelastic model. *(c)* Relaxation time λ, *(d)* viscosity factor μ_0, and *(e)* power law index n as a function of concentration. Two different trends for μ_0 and n indicate the structural transition of solutions from the semi-dilute to concentrated regime.

weight. The rheological properties of all polymeric solutions are characterized by a stress-controlled rheometer (RFS3, TA Instruments). Fig. 15*(a)* shows the shear viscosity μ of all fluids as a function of shear rate $\dot{\gamma}$. All fluids exhibit shear-thinning viscosity with the exception of M9 buffer solution which exhibits water-like behavior. This non-Newtonian viscosity behavior is well captured by an empirical power law fluid model of the type $\mu = \mu_0|\dot{\gamma}|^{n-1}$, where μ_0 is the viscosity factor and n is the power law index.

Fluid relaxation times are obtained by fitting the stress relaxation data with the generalized linear viscoelastic model of a single relaxation time of the type $G(t) = G_0 e^{-t/\lambda}$, where $G(t)$ is the fluid shear modulus and λ is the longest relaxation time of the fluid. Figure 15*(b)* shows the data and a sample fitting and the values of λ are shown in Fig. 15*(c)*. Figure 15*(d)* shows the values of μ_0 as a function of XG polymer concentration. The different slopes found in Fig. 15*(d)* represent two distinct polymer concentration regimes,

namely the semi-dilute and concentrated regimes. The transition from the semi-dilute to the concentrated regime seems to happen near or around 3000 ppm and it is commonly interpreted as a structural transition (Rodd et al., 2000; Doi and Edwards, 1988). In concentrated solution, the shape and dynamic properties of polymer networks dominate flow behaviors; in semi-dilute solution, the hydrodynamic interactions among individual polymers dominate flow behaviors (Doi and Edwards, 1988). We note that the power law index n of xanthan gum solutions also shows two regimes (Fig. 15*(e)*) due to the aforementioned structural transition (Wyatt and Liberatore, 2009). We note that there is no expectation for concentration transition to be reflected by the change in slope of relaxation time λ in Fig. 15*(c)*.

Particle tracking methods are used to measure the velocity fields generated by the nematodes swimming in the various polymeric fluids. Figure 14*(c)* and *(d)* show normalized velocity fields for *C. elegans* swimming in semi-dilute (2000 ppm) and concentrated (4000 ppm) XG solutions. Velocities for each solution are normalized by their respective root-mean-square velocities and then scaled by the maximum between the two regimes. These normalized streamlines are color-coded to highlight regions of high (red) and low (blue) flow. We find large recirculating regions around the nematode's body and regions with large extensional (or straining) components. The flow structures are relatively similar for both cases, but we find differences around the nematode's midsection, where relative velocities in the concentrated case are nearly twice as large as those in the semi-dilute case and are predominately in the normal direction. We will discuss this feature later in the manuscript.

4.2. Polymer Concentration Effects

We begin by analyzing the swimming kinematics of *C. elegans* in XG solutions as a function of polymer concentration. Figures 16*(a)*-*(c)* show the nematode's beating frequency f, wave speed ν_p, and swimming speed U as a function of concentration, respectively. As

the polymer concentration increases, we find a gradual and monotonic decay in the nematode's wave speed ν_p and a decay in beating frequency f below 3000 ppm followed by a plateau at higher concentrations (Fig. 16*(a)* and *(b)* respectively). This decrease in such kinematic functions is expected as a result of increased viscosity as polymer concentration increases (Fig. 15*(d)*).

Figure 16*(c)* shows that the nematode's swimming speed U remains relatively constant for polymer concentrations below 3000 ppm. Surprisingly, however, we find a sudden increase in U for concentrations above 3000 ppm. The values of U are maintained around 0.15 mm/s in semi-dilute solutions but they quickly rise by 65% to about 0.25 mm/s in concentrated solutions despite a significant increase in solution viscosity. As expected, the swimming speed ultimately decreases as the concentration is further increased due to the nematode's finite power output (Shen and Arratia, 2011). An increase in U with viscosity has been previously reported for microorganisms moving in structured gel-like media, but the mechanisms are still not well understood (Berg and Turner, 1979; Schneider and Doetsch, 1974). A recent theoretical work suggests that such increase may be due to the presence of polymer networks in the media and that microorganisms may be able to push against such quasi-static networks and move more efficiently (Magariyama and Kudo, 2002). However, because of the large difference in length scales between the nematode ($\approx$ 1 mm) and the polymer networks ($\approx 10\ \mu$m) as well as the lack of quasi-static flow fields in the concentrated regime (Fig. 14*(d)*), this notion does not adequately explain the observed propulsion enhancement. In what follows, we will show that the propulsion enhancement for *C. elegans* swimming in concentrated polymer solutions is related to shear-induced fluid anisotropy.

4.3. Swimming Speed & Fluid Rheology

To better understand the mechanisms governing of this unusual enhancement in U, we investigate the effects of both fluid viscosity and elasticity on the nematode's swimming

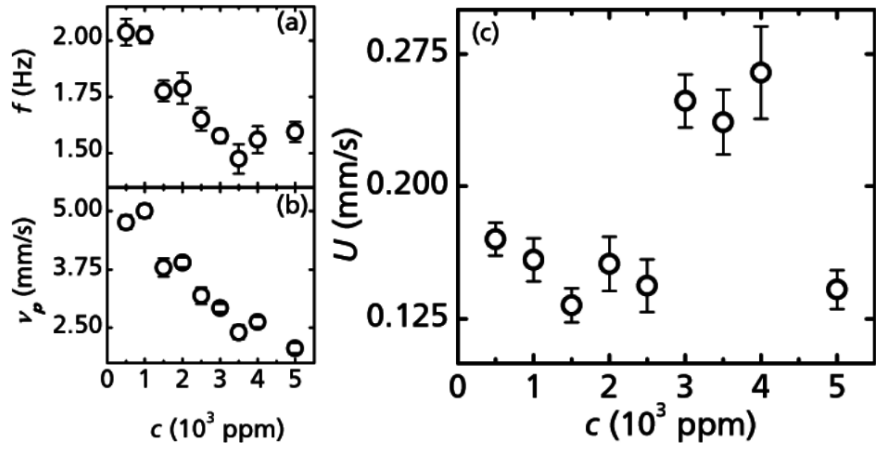

Figure 16: *(a, b)* Swimming frequency f and wave speed v_p as a function of concentration. *(c)* Swimming speed as a function of concentration. Swimming speed exhibits a rapid increase as the solution enters the concentrated regime.

speed. Figure 17*(a)* and *(b)* show the values of U as a function of fluid viscosity coefficient μ_0 and power law index n. Note that the transition from semi-dilute to concentrated regime in the XG solutions occurs at $\mu_0 \approx 1$ Pa·s and $n \approx 0.3$, as shown in Fig. 15*(d)* and *(e)*. Results show that the nematode is able to maintain a constant swimming speed ($\approx$ 0.15 mm/s) for $\mu_0 \lesssim 1$ Pa·s but exhibits a rapid increase to $U \approx 0.25$ mm/s for $\mu_0 \gtrsim 1$ Pa·s (Fig. 17*(a)*). This corresponds to an increase in swimming speed of about 65% as the fluid viscosity increases. As expected, further increase in viscosity beyond $\approx$ 2 Pa·s reduces swimming speed, which suggests that the enhancement in swimming speed is bounded by the nematode's limited power output (Shen and Arratia, 2011). The effects of shear thinning on the nematode's swimming speed (Fig. 17*(b)*) echo the similar pattern found with μ_0. That is, the swimming speed is abruptly enhanced for XG solutions corresponding to $n \gtrsim 0.3$; below such value, the nematode's swimming speed remains relatively constant.

Due to the relatively high polymer concentration and the formation of polymer networks, viscoelastic effects are expected in semi-dilute and concentrated XG solutions. Fluid elasticity is known to strongly affect the swimming behavior of microorganisms (Fu et al., 2009; Lauga and Powers, 2009; Shen and Arratia, 2011). For the case of *C. elegans*, it has

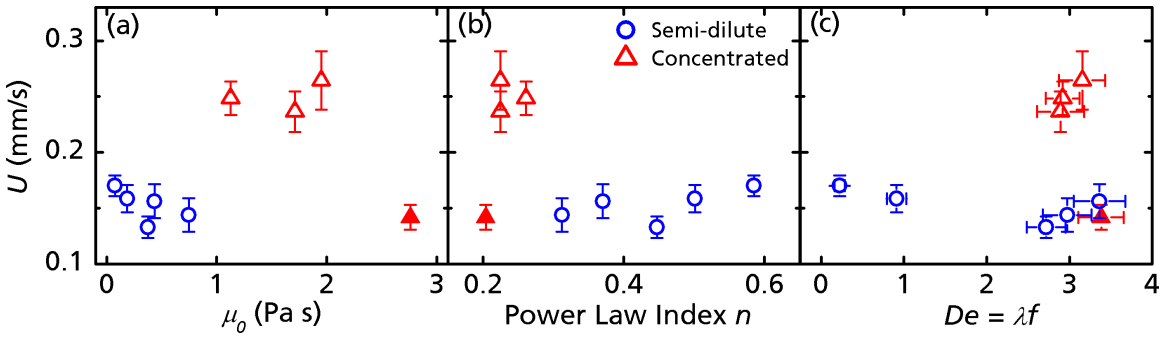

Figure 17: (Color Online) Nematode's swimming speed as a function of *(a)* viscosity factor, *(b)* power law index, *(c)* and Deborah number or fluid elasticity (see text).

been recently shown the swimming speed decreases as fluid elasticity increases *in dilute solutions* (Shen and Arratia, 2011). Viscoelastic effects are best investigated by introducing the Deborah number, defined as $De = \lambda f$, where λ is the fluid relaxation time and f is the nematode's beating frequency. The Deborah number represents the ratio of the time-scale of the fluid "fading memory" to the period of flow induced during undulatory swimming (Lauga and Powers, 2009). Note that $\lambda = 0$ for Newtonian fluids and $De \to \infty$ for an elastic solid. Figure 17*(c)* shows the nematode's swimming speed as a function of De. We find that the rapid increase in the nematode's swimming speed is not determined by De (or fluid elasticity) but rather the transition from semi-dilute to concentrated fluid structure.

4.4. Discussion

Our data show a rapid increase in the swimming speed of *C. elegans* as the XG polymer concentration increases beyond 3000 ppm, which roughly corresponds to the transition from the solution semi-dilute to the concentrated regime. The main bulk rheological parameters such as viscosity factor μ_0, power law index n, and fluid relaxation time (elasticity) λ do not fully capture the observed phenomenon. This suggests that the polymer networks present in the concentrated polymeric fluids may be responsible for this enhancement in propulsion speed.

In order to identify the mechanism behind the enhancement of swimming speed, we examine the normalized flow field streamlines shown in Fig. 14*(c)* and *(d)* for nematodes swimming in semi-dilute (2000 ppm) and concentrated (4000 ppm) XG solutions. Both fields possess the similar flow structures. However, in the concentrated regime, we find a region of high relative velocity that is predominantly oriented normal to the nematode's body, whereas in the semi-dilute regime, this region is absent. Note that simply modulating fluid viscosity would uniformly change velocities in the field in all directions; that is, the velocity fields would scale linearly with viscosity. This is clearly not that case in the concentrated regime, as the velocities normal to the nematode's mid section are larger relative to the tangential velocities. This indicates a more complex relationship between the swimmer and the networks in the polymer solution. As discussed earlier (see Fig. 15*(d)* and *(e)*), the fluid internal structure is sensitive to polymer concentration, particularly as the XG concentration increases from the semi-dilute to the concentrated regime (Rodd et al., 2000; Doi and Edwards, 1988). Our results indicates that the flow behavior of semi-dilute XG solutions is dominated by the hydrodynamic interaction among polymer molecules, while the flow behavior of concentrated solutions is dominated by molecule shape and dynamic properties of the polymer networks (Doi and Edwards, 1988).

We quantify the observed differences in the flow field by computing the probability distribution function (PDF) of the tracer particle velocities embedded in the flow. PDF plots are shown in Fig. 18*(a)* and *(b)* for a semi-dilute (2000 ppm) and a concentrated (4000 ppm) XG solution, respectively. The PDFs are decomposed into tangential and normal directions, which are computed with respect to the nematode's swimming direction. Here, the tangential direction corresponds to the nematode's swimming direction while the normal direction is perpendicular to the swimming direction. The area around the PDF's central peak, where velocity magnitudes $|v|$ are small, isotropic, and dominated by noise, represents the flow field far away from the swimming *C. elegans*. The measurements of interest are at the PDF's tails, which correspond to regions of the flow field close to the nematode.

Near the nematode's body, the velocity distributions exhibit exponential decay tails, indicating the dominant role of convection arising from the swimming motion. The solid lines represent an exponential fit of the decay tails of the form $P(v) = P(v)_0 + Ae^{B\frac{v}{v_{max}}}$, where $P(v)$ is the probability density function (PDF) of velocity, v and v_{max} are the tracer particles' speed and maximum speed in the flow field, A is a fitting coefficient, and B is the decay slope. Results show that in the semi-dilute solution, both the normal and tangential velocity components show roughly the same decay slope: $B = -7.76, \ -7.07$ respectively. A different trend, however, is found for the velocity distribution in concentrated solutions. While both tangential and normal components show exponential tails near the nematode's body (high velocities), we note an anisotropic distribution the decay rates of velocity components. The decay slopes for the tangential and normal directions are $B = -9.82, \ -5.85$ respectively, indicating velocities in the tangential direction decay faster at high velocities than those in the normal direction. This implies that for nematodes swimming in concentrated XG solution, there are regions where the fluid has a relative enhancement in momentum in the normal direction. At low Reynolds number, where fluid momentum is instantaneously dissipated, higher fluid speed and momentum along the normal direction require stronger driving force from the swimmer. Consequently, the nematode experiences an enhanced drag in the normal direction. Our data suggest that the nematode's motion is causing an anisotropic mechanical response in the fluid (in concentrated solutions), which enhances the normal viscous drag on the nematode and leads to the nematode's swimming speed enhancement.

Next, we examine the physical properties of the XG solutions in the semi-dilute and concentrated regimes. As mentioned before, XG is a semi-rigid, rod-like polymer, which has a molecular weight (MW) of approximately 2×10^6, a hydrodynamic length of approximately 1.5 μm and a contour length of approximately 2.0 μm (Zirnsak et al., 1999). At equilibrium, it has been established that for semi-rigid rod-like polymers, the fluid structure can transition from an isotropic fluid to an anisotropic nematic liquid crystal as the

polymer concentration increases in the solvent (Tracy and Pecora, 1992; Lim et al., 1984). This transition occurs in the concentration regime $\frac{4(MW)}{N_A d\ell^2} \lesssim c \lesssim \frac{6(MW)}{N_A d\ell^2}$, where d and ℓ are the diameter and hydrodynamic length of the xanthan gum macromolecule respectively, MW is its molecular weight, N_A is Avogadro's number, and c is the polymer concentration (Tracy and Pecora, 1992). Here, $d \approx 2$ nm, $\ell \approx 1.5$ μm, and $MW \approx 2 \times 10^6$ Da. For the xanthan gum solutions investigated here, this corresponds to a transition between concentrations of approximately 2900 and 4400 ppm. It is between these concentrations that we observe changes in the viscosity coefficient and power law index trends (Fig. 15*(d)* and *(e)*) and in the nematode's swimming speed (Fig. 16*(c)*). It is believed that this transition occurs because these slender macromolecules can no longer freely rotate; rather, their interactions are becoming increasingly confined and crowded by adjacent molecules. As the molecules become more crowded, the parallel component of the molecule's diffusion coefficient $D_{\parallel}$ becomes much greater than its perpendicular component $D_{\perp}$ because these rod-like molecules are more prone to slide past each other than to rotate (Dobrynin et al., 1995).

The nematode's motion, however, disrupts the aforementioned equilibrium picture by introducing shear stresses to the system. The introduction of shear stresses in a rod-like polymeric solutions (e.g. XG fluids) causes molecules to align with the direction of shear due to their anisotropic drag (Song et al., 2006; Zirnsak et al., 1999); that is, a rod-like molecule moves more easily along its length than normal to it. This alignment gives rise to the shear thinning viscosity behavior of XG solutions (Fig. 15*(a)*). The shear stresses introduced in the fluid by the nematode are also able to align these molecules, at least locally, and can lead to the formation of local nematic structures at high concentrations (Dobrynin et al., 1995). The combination of these local nematic structures with the anisotropic diffusivity present only in the concentrated regime gives rise to the enhanced drag in the normal direction experienced by the nematode (Fig. 18*(b)*).

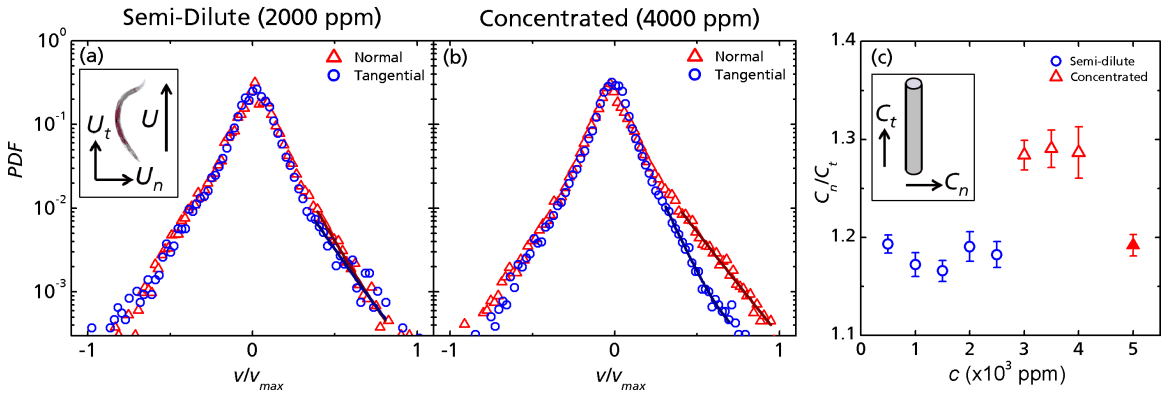

Figure 18: (Color Online) Probability distribution functions (PDF) of velocity components of tracer particles in *(a)* semi-dilute and *(b)* concentrated solutions. PDFs are computed at the same phase and are normalized by the total number of particles in the flow field. The blue circles (○) and red triangles (△) represent the tangential and normal components of the velocity vectors with fitted exponential decay slopes. Inset: a schematic of nematode's velocity components. *(c)* The effective drag coefficient ratios $C_n/C_{t,\,eff}$ for semi-dilute (blue circles) and concentrated (red triangles) solutions. Inset: an illustration of drag coefficients for a slender cylinder.

In order to elucidate the mechanism discussed above, i.e. the relative enhancement in drag in the normal direction, we estimate the drag coefficient ratio C_n/C_t using resistive force theory (RFT) (Gray and Hancock, 1955) along with our kinematic data. We note that RFT is only valid for Newtonian fluids and its used here is solely to illustrate a possible mechanism. The ratio of the nematode's length ($\approx$ 1 mm) to its diameter ($\approx$ 80 μm) is approximately 12. Hence, in the limit of low *Re*, *C. elegans* may be treated as a slender body moving in a viscous fluid. An expression for the swimming speed U for an undulating filament was proposed by Gray and Hancock (Gray and Hancock, 1955) and is given as $U = 2\pi^2 \left(\frac{f^2 A^2}{\nu_p}\right)\left(\frac{C_n}{C_t} - 1\right)$ where ν_p, A, and f are the wave speed, beating amplitude, and frequency respectively. The quantity C_n/C_t is the drag coefficient ratio where C_n and C_t are normal and tangential drag coefficients (Gray and Hancock, 1955). The presence of polymer networks in the fluid can affect this drag coefficient ratio (Francois et al., 2008), and we use the above expression to approximate an *effective* drag coefficient ratio, $C_n/C_{t,\,eff}$. While these estimates cannot be quantitatively compared to those for a Newto-

nian fluid, they can provide valuable insight into the degree of anisotropy present in the fluid micro-structure.

Figure 18*(c)* shows the ratio $C_n/C_{t,\,eff}$ as a function of XG concentration estimated by incorporating experimentally measured kinematics (i.e. U, v_p, A, and f) (Gray and Hancock, 1955). We find a rapid increase in $C_n/C_{t,\,eff}$ as the polymer concentration increases beyond 3000 ppm, where the solutions transition from the semi-dilute to the concentrated regime (Fig. 15*(d)* and *(e)*). This suggests a relative increase of C_n compared to C_t for polymer concentration $>$ 3000 ppm. This relative enhancement in the normal component of the drag coefficient C_n is corroborated by measurements of the velocity fields (Fig. 14*(c)* and *(d)*) and the PDFs of their velocity distributions (Fig. 18*(a)* and *(b)*).

CHAPTER 5 : Swimming in viscoelastic fluids under confinement

By introducing a far-field no-slip boundary condition, one can mimic natural biological processes such as bacteria moving through vesicles in the circulatory system and sperm cells swimming through millimeter-scale fallopian tubes (Colburn, 1986); both of these systems contain non-Newtonian fluids (blood and mucus, respectively). Building off our above argument that non-Newtonian fluids are the most appropriate model system for studying biological locomotion, we believe a necessary component of studying low Reynolds number swimmers is a systematic experimental investigation of swimming under confinement in non-Newtonian fluids.

An analytical study (Katz, 2003) and a numerical computation (Münch et al., 2016) using an infinite waving sheet in the presence of solid boundaries have proposed that an undulatory swimmer should swim faster under confinement in a Newtonian fluid. Several studies have shown that hydrodynamic wall interactions can also lead to aggregation in Newtonian fluids (Li and Ardekani, 2014), and modified aggregation in viscoelastic fluids (Yazdi et al., 2014, 2015). Additionally, work with *C. elegans* has shown that the presence of solid boundaries can lead to a modulated swimming gait, particularly a decrease in amplitude in Newtonian fluids (Schulman et al., 2014). However, there is a lack of experimental data on the combined effects of viscoelasticity and confinement on swimming behavior. We therefore combine effects of confinement and fluids with viscoelastic and shear-thinning rheology and examine their fundamental effects on the kinematics of an undulatory swimmer. For *C. elegans* swimming through a thin channel, as the walls of the channel approach the characteristic transverse length-scale of the nematode's swimming gate, defined as the head amplitude, we expect modifications of the flow field around the swimmer, which in turn will modify fluid stresses and simultaneously the nematode's swimming behavior.

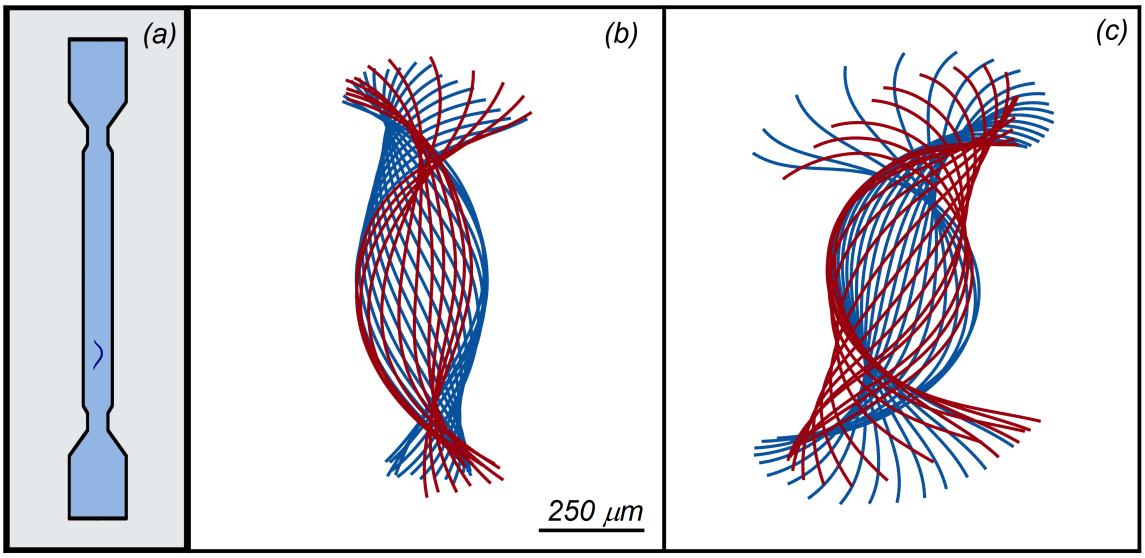

Figure 19: *(a)* Schematic of confinement channel geometry. *(b)* Nematode body shapes during one beating cycle in a viscosified Newtonian fluid under confinement. *(c)* Nematode body shapes during one beating cycle in a viscoelastic fluid under confinement.

5.1. Experimental Methods

Swimming experiments in Newtonian and non-Newtonian fluids are performed using the nematode *C. elegans*. These nematodes are characterized by a relatively long and quasi-cylindrical body shape and are approximately 1 mm in length and 80 μm in diameter; their genome has been completely sequenced (Brenner, 1974) and a complete cell lineage has been established (Byerly et al., 1976). *C. elegans* are equipped with 95 muscle cells that are highly similar in both anatomy and molecular makeup to vertebrate skeletal muscle (White et al., 1986). Their neuromuscular system controls their body undulations, allowing *C. elegans* to swim, dig, and crawl through diverse environments. The wealth of biological knowledge accumulated to date makes *C. elegans* an ideal candidate for investigations that combine aspects of biology, biomechanics, and the fluid mechanics of propulsion.

Experiments are performed in thin, fluid-filled acrylic channels 30 mm long and 1.6 mm deep covered by a thin, glass microscope cover slip (Fig. 19*(a)*). The width of the channels

ranges from 1.0 mm to 1.8 mm. The smallest channel width is set by the maximum amplitude of the nematode, which is approximately 0.25 mm, such that there is no direct contact with the wall. Additionally, free swimming experiments are performed where the nematodes are laterally unrestricted. Ideal recordings are of the nematode swimming parallel to the channel walls and in the geometric center of the channel. Consequently, recordings where the nematode directly interacts with the wall or where the nematode swims at an angle with the wall greater than 15 degrees are also discarded. On average, 17 individuals are recorded for each combination of fluid and channel width.

We image their swimming motion using standard bright-field microscopy (Infinity K2/SC microscope with an in-system amplifier, a CF-3 objective, and an IO Industries Flare M180 camera at 150 frames per second). The depth of focus of the objective is approximately 20 µm and the focal plane is set on the longitudinal axis of the nematode body. The nematode beats primarily in the observation plane; the out-of-plane beating amplitude of *C. elegans* is less than 6% of the amplitude of its in-plane motion (Sznitman et al., 2010b). All data presented here pertain to nematodes swimming at the center of the fluidic chamber and out-of-plane recordings are discarded to avoid nematode-wall interactions.

5.1.1. Swimming kinematics

The nematode's swimming kinematics are obtained from videos using in-house software (Sznitman et al., 2010c). The software extracts the nematode's centroid position and body shape-line, and computes quantities such as swimming speed U and body curvature κ. Swimming speed is obtained by differentiating the nematode's centroid position with time, and we define the positive y-axis as the swimming direction. The body curvature is defined as $\kappa = \delta\phi/\delta s$, where ϕ is the angle between a fixed reference axis and the tangent to the body shape-line, at each point s along the body contour, where s is an arc length parameterization. The evolution of $\kappa(s,t)$ over many beating cycles reveals periodic lines that propagate in time from head ($s = 0$) to tail ($s = L$), illustrating the characteristic traveling

wave of undulatory swimming (Sznitman et al., 2010b; Gagnon et al., 2013). The slope and rate of occurrence of these lines represent wave speed c and beating frequency f, respectively. In water-like buffer solutions, we find $U \approx 0.35$ mm/s, $f \approx 2$ Hz, and $c \approx 5$ mm/s. The Reynolds number, defined as $Re = \rho UL/\eta$, is approximately 0.35, where L is the nematode's length (1 mm), ρ is the fluid's density (10^3 kg/m^3), and η is the fluid's viscosity (1 mPa·s), indicating that viscous forces dominate the flow.

5.1.2. Particle tracking

We measure the velocity fields generated by swimming *C. elegans* in both Newtonian and non-Newtonian fluids by seeding the working fluids with 3.1 µm polystyrene tracer particles, which are tracked continuously for the entire duration of the experiment using in-house codes. These tracer particles are dilute ($< 0.5\%$ by volume) and do not alter the properties of the fluid. We image the nematodes swimming through this seeded fluid for 6 to 10 cycles, with each swimming cycle (or period) containing 60 phases. Because *C. elegans* beat at a constant frequency, we can phase-average the data and obtain spatially resolved velocity fields. We note that data points for each phase are averaged into gridded spaces of size 20 µm. We estimate the full 3D shear rate tensor by applying a correction factor developed expressly to estimate the errors present in planar particle tracking data; without this correction factor, we would underestimate the shear rate magnitude and therefore the strength of viscoelastic effects (Montenegro-Johnson et al., 2016).

5.1.3. Fluid Properties

The viscoelastic fluids were made by adding carboxymethylcellulose sodium salt (CMC) to water (Sigma-Aldrich C5678). CMC is a flexible, long-polymer with fluid relaxation times λ of 0.8 and 2.3 at concentrations of 3000 and 5000 ppm by weight, respectively (Shen and Arratia, 2011). These times were calculated by measuring the fluid shear modulus $G(t)$ over time and fitting the data to the generalized linear elastic model of the form

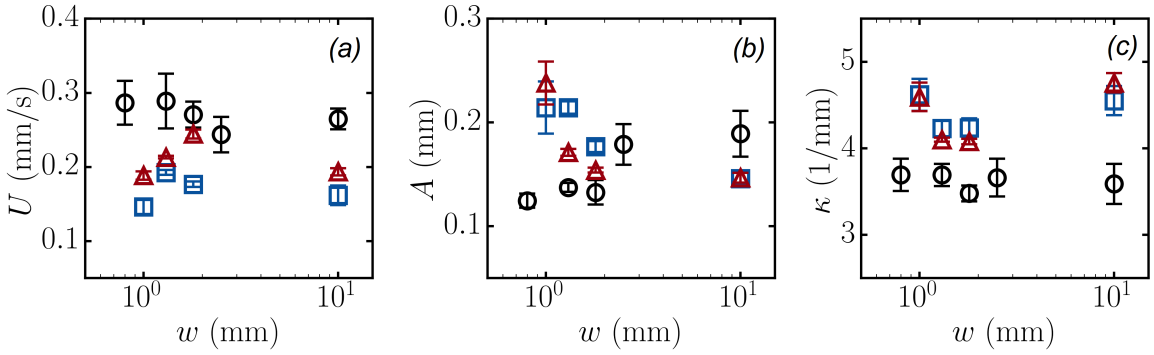

Figure 20: *(a)* Swimming speed U, *(b)* amplitude A, *(c)* curvature κ, and *(d)* Strouhal number St for viscosity Newtonian solution (black circles), 3000 ppm CMC viscoelastic solution (red triangles), and 5000 ppm CMC viscoelastic solution (blue squares) as a function of channel width and therefore confinement.

$G(t) = G_0 e^{-t/\lambda}$. These fluids have effective viscosities of 100 mPa·s and 400 mPa·s for the 3000 ppm and 5000 ppm version respectively. At these dilute concentrations, the shear-thinning effects in the CMC are negligible (Benchabane and Bekkour, 2008). Lastly, a viscosity-matched aqueous Ficoll PM 400 solution with a concentration of 23% by weight was prepared as a Newtonian buffer solution, which has a viscosity μ of approximately 50 mPa·s, similar to the viscosity of the 3000 ppm CMC solutions (Sigma-Aldrich F4375).

5.2. Experimental Results

The presence of viscoelasticity substantially modifies the body shape of *C. elegans* under confinement. Figure 19*(a)* and *(b)* show the body shapes over one cycle for a nematode swimming through a 1.3 mm channel in a Newtonian and viscoelastic fluid respectively. The shape of the worm's body in the viscoelastic case suggests a larger amplitude and body curvature. We therefore begin by quantifying the kinematics of swimming *C. elegans* in both Newtonian and viscolelastic fluids under confinement conditions ranging from free-swimming to swimming through channels approximately equal to the length of the nematode.

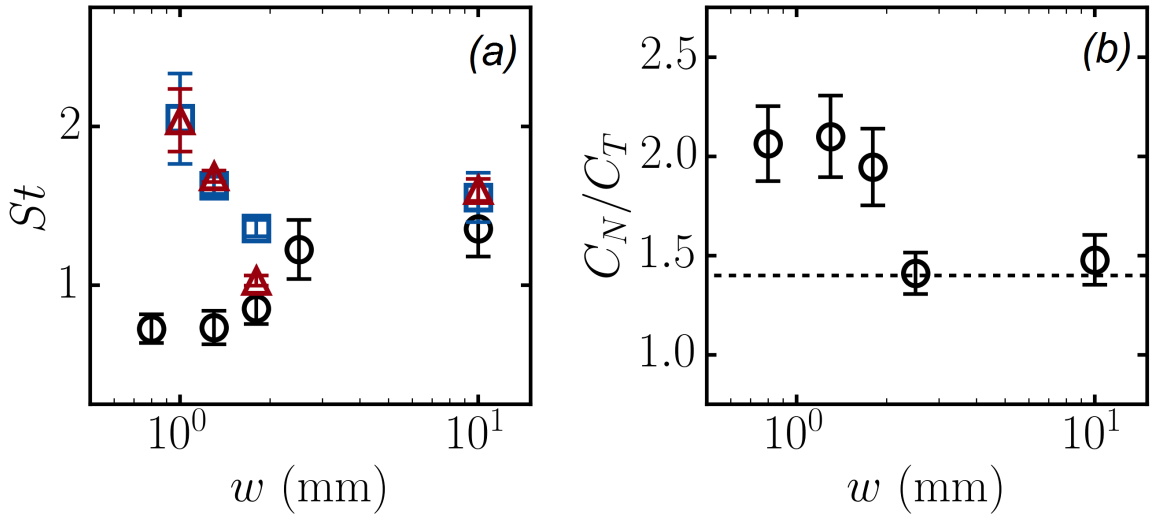

Figure 21: *(a)* The Strouhal number $St = fA/U$ with decreasing channel width *(b)* The estimated drag coefficient ratio C_N/C_T for Newtonian fluids with decreasing channel width.

5.2.1. Kinematics

In a Newtonian fluid, we find that swimming speed increases with thinner channels and therefore with increasing confinement. We also find that the swimmer's amplitude decreases while its curvature remains relatively constant. Figure 20 summarizes these results for swimming in Newtonian fluids (black circles) for *(a)* swimming speed, *(b)* amplitude, and *(c)* curvature. Previous analytical results for an infinite undulatory sheet have suggests that swimming speed should indeed increase with increasing confinement (Katz, 2003).

On the other hand, results in the two viscoelastic solutions of CMC show a significant departure from our observation in Newtonian fluids (Fig. 20, 3000 ppm CMC: red diamonds and 5000 ppm CMC: blue squares). We find that viscoelasticity increasingly hinders the swimming speed of *C. elegans* with increasing confinement. We also notice that unlike the Newtonian case, the viscoelastic medium seems to increasing the beating amplitude of *C. elegans* despite increasing confinement. It follows that increasing viscoelastic stresses are likely responsible for these modifications in swimming gait.

The viscoelastic effects on the swimming speed and on the amplitude of the swimmers is best described by Strouhal number (St). The Strouhal number describes the transient flow patterns in an oscillating system. In this case, it is used to compare the rate of undulatory motion to the rate of forward motion of the swimmer, and is defined as $St = fA/U$. Figure 21*(a)* shows the Strouhal number as a function of the channel width in the case of each of the three fluids (Ficoll, 3000 ppm CMC, and 5000 ppm CMC). The Strouhal number is approximately equal irrespective of the presence of viscoelasticity for a freely swimming nematode. As the swimmer becomes more confined, however, there is a very clear separation where the Strouhal number in the Newtonian case slowly decreases while, in the viscoelastic cases, the Strouhal number steadily increases with decreasing channel width. This suggests that in viscoelastic fluids, worms are producing increasing transverse motion in viscoelastic fluids under confinement, but that additional transverse motion is poorly converted into increased forward translation. For Newtonian fluids, this is not the case; worms require less transverse motion for slightly increased forward translation, potentially reducing their cost of swimming when under confinement.

We also have computed an estimate of the effective drag coefficient ratio C_N/C_T for *C. elegans* swimming in Newtonian fluids under confinement from a simple resistive force theory model, which relates the swimming speed of an undulatory swimmer to its body geometry and frequency (Hancock, 1953):

$$U = 2\pi^2 \frac{f^2 A^2}{c} \left(\frac{C_N}{C_T} - 1 \right), \tag{5.1}$$

where U is swimming speed, c is wave speed, f is frequency, and A is amplitude. Rewriting this equation and grouping non-dimensional terms we find:

$$\frac{C_N}{C_T} - 1 = \frac{1}{2\pi^2} \frac{Uf\lambda}{f^2 A^2} = \frac{1}{2\pi^2} \frac{\lambda}{A} \frac{1}{St}, \tag{5.2}$$

where $St = fA/U$ is the Strouhal number and λ is the wavelength nematode. Here, we see that the drag coefficient ratio is only dependent on the inverse of the Strouhal number and a ratio of the waveform of the swimming gait λ/A; decreasing St implies increasing C_N/C_T and more efficient locomotion. The results are shown in Figure 21*(b)* for Newtonian fluids, which suggest a significant increase in C_N/C_T with decreasing channel width w; the dashed line represents previous experimental measurements of $C_N/C_T \approx 1.4$ for freely-swimming *C. elegans* (Sznitman et al., 2010b). These results therefore suggest that *C. elegans* are kinematically more efficient swimmers under confinement in Newtonian fluids, a result previously proposed analytically (Katz, 2003) and numerically (Münch et al., 2016). This also suggests the inverse result in viscoelastic fluids under confinement; *C. elegans* appear substantially less kinematically efficient.

5.2.2. Flow fields and quantifying the role of elasticity

One possible explanation for the observed deviations in Strouhal number St between Newtonian and viscoelastic fluids is that the extent and shape of the flow field varies depending on the viscoelasticity of the fluid and that these modifications lead to significantly modified shear rates and in turn large elastic stresses. We therefore must evaluate the the flow fields surrounding a swimming under confinement using particle tracking velocimetry in order to quantify the role of extensional flow and elasticity for low Reynolds number swimmers in viscoelastic fluids under confinement. Because we are interested in the role of viscoelastic effects, and because the viscoelastic effects should be most prominent in regions of high shear rate, we select the phases or snapshots of the swimming cycle which have the highest average shear rate around *C. elegans*. This generally corresponds to the moment in a swimming cycle in which the worm is curled into a 'C'-shape and then begins to straighten its body.

We analyzed the flow fields around the worm at this phase of maximum shear rate in the swimming cycle; figure 22 shows both the instantaneous streamlines and velocity magni-

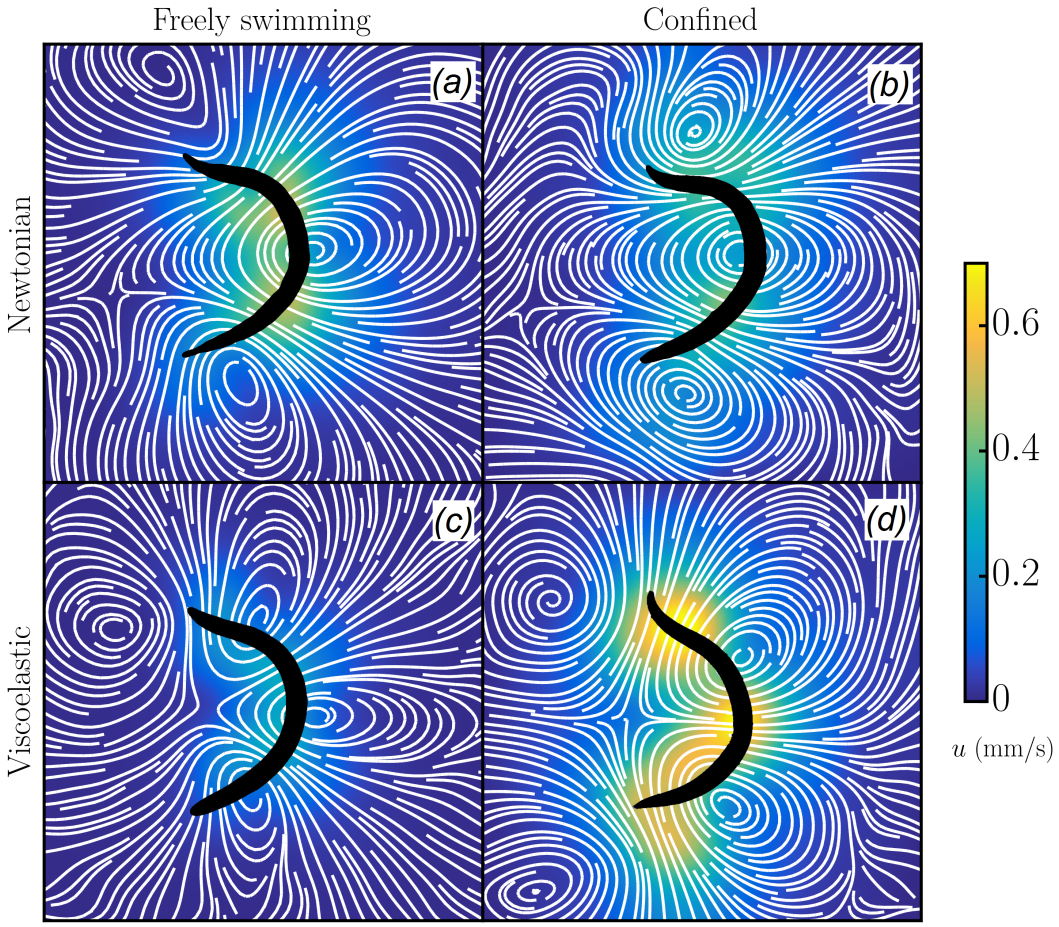

Figure 22: Streamlines and fluid velocity fields for *C. elegans* swimming under the following conditions: *(a)* Newtonian freely swimming, *(b)* Newtonian confined, *(c)* viscoelastic free-swimming, and *(d)* viscoelastic confined.

tude for each case: Newtonian, confined and unconfined, and viscoelastic, confined and unconfined. First, freely swimming *C. elegans* in a Newtonian fluid appears to produce large velocity magnitudes compared to the confined case. This is consistent and expected due to decrease in the average transverse velocity fA observed most easily through the decrease in the Strouhal number (Fig. 21). There also appears to be a decrease in the size of the head vortex and it has shifted from the upper left of the worm's head in the free-swimming case to the upper center of the flow field in the confined case. Next, addition of viscoelasticity substantially changes the structure of the flow field for the free swimming case; in particular, we can now see four well-defined vortices in the viscoelastic case and a substantially more symmetric hyperbolic point located significantly closer to the worms body. We also note that the overall fluid speed is lower than the Newtonian case. This reduction in fluid speed is consistent with previous experimental results, which demonstrated that viscoelasticity substantially enhances the decay of the flow field away from the swimmer's body while also decreasing the transverse and translational velocities of the swimmer body (Shen and Arratia, 2011).

Lastly, we can examine the effects of combining both a viscoelastic medium and confinement. A fairly symmetric hyperbolic point is located just inside the concave region of the worm's body; there are only two vortices attached to the body and the outward motion of the head and tail appear to form the unstable manifold of the hyperbolic point, while rightward flow from the wall and the leftward movement of the worm's midsection produce the stable manifold. Fluid velocity in the entire field is largely confined to these regions (bright yellow). This implies a substantial amount of fluid stretching and therefore elastic response from the viscoelastic fluid. This structural change in the flow field, which suggests a substantial increase in elastic stresses near the body of the worm and provides a possible mechanism for the radical change in swimming gait shown through St and significant reduction in swimming speed U.

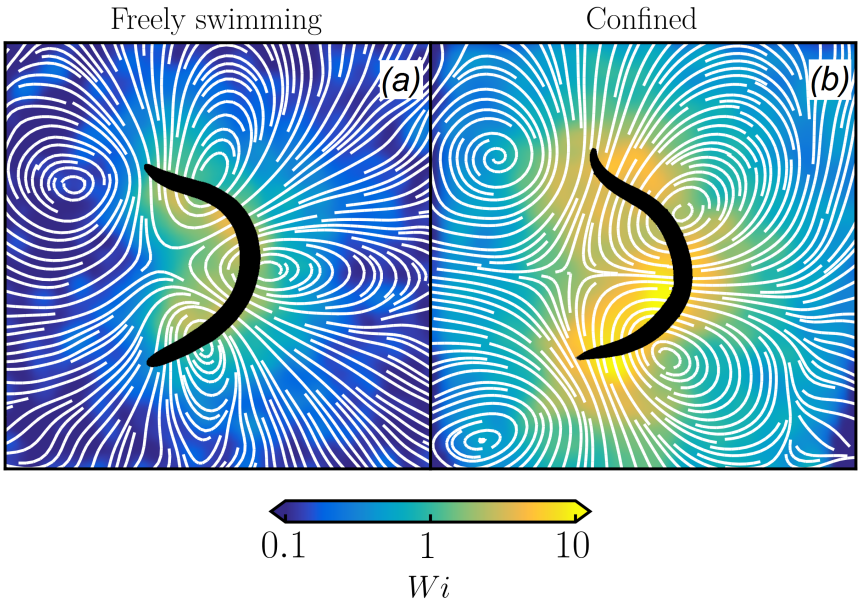

Figure 23: Weissenberg number Wi field for *(a)* freely swimming and *(b)* confined *C. elegans* in a viscoelastic fluid with a relaxation time of $\lambda = 0.8$ s.

In order the quantify the role of elasticity, we can consider two non-dimensional numbers: the Deborah number $De = 2\pi f\lambda$ and the Weissenberg number $Wi = \dot{\gamma}\lambda$, where λ is the longest relaxation time of the fluid, found through creep relaxation measurements in a cone and plate rheometer. Though both numbers can be viewed as a ratio of timescales, they probe different features of the interaction between the swimmer and the fluid. First, De quantifies the frequency at which the flow is driven, in this case the beating frequency of *C. elegans*, to the fluid relaxation time. Values of $De \sim 1$ imply that each new beating cycle of the worm occurs in the presence of the elastic stresses generated by the previous cycle, whereas $De \ll 1$ suggests that the fluid has ample time to relax between beating cycles. In both the confined and unconfined viscoelastic flow fields, $De \approx 8$. This indicates that elastic effects are present, but is unable to help elucidate how the presence of boundaries modifies the swimming gait. On the other hand, Wi quantifies the relative strength of elastic stresses to viscous stresses. More explicitly, this can be written as $Wi = \lambda\mu\dot{\gamma}^2/\mu\dot{\gamma}$, where the numerator is derived from the first normal stress difference N_1. Now, it is clear

that Wi quantifies the fluid deformation relative to the fluid dissipation and relaxation. When $Wi \geq 1$, it implies the presence of significant elastic stresses. In the case of our flow field comparisons, the viscoelastic fluid is the same for both the free-swimming and confined cases and has a relaxation time of $\lambda = 0.8$ s; therefore, the magnitude of Wi can also be viewed as a proxy for a comparison of the shear rate magnitude $\dot{\gamma}$.

Next, we locally estimate Wi for both the freely swimming and confined viscoelastic cases, shown in Fig. 23. Immediately, we can see that the average Wi is substantially larger for the confined case, and the region of $Wi \geq 1$ envelopes the entire body of the swimmer. Furthermore, the regions of highest Wi for the confined case near the stable and unstable manifolds of the hyperbolic point are roughly a factor of two larger than the maximum Wi for the free-swimming case. This is concrete evidence that the presence of boundaries can substantially magnify the effects of fluid elasticity. In the case of *C. elegans*, the increased elasticity due to the walls dramatically modifies its swimming gait, resulting in larger amplitude undulations yet a slower swimming speed.

CHAPTER 6 : Application of locomotion assays to the study of genetic disease

We are now well-equipped to use a swimming assay incorporating both kinematics (e.g. swimming speed) and dynamics (e.g. bending force) to examine the swimming behavior of four groups of *C. elegans*: control groups N2 (wildtype) and the long-lived mutant *daf-2(e1370)*, a diseased group *smn-1(ok355)*, and a rescue group *smn-1(ok355);daf-2(e1370)*. By observing this periodic motion during forward swimming, we are able to detect statistically significant differences between the diseased and rescue groups for three important factors: kinematic efficiency, bending force, and mechanical power. Kinematic efficiency describes the ability of the nematode to translate its traveling wave into forward propulsion, bending force indicates the forces required to bend the nematode's body into the observed configurations, and mechanical power represents the rate of energy expenditure for the nematode's forward progress. Although *smn-1(ok355)* animals display impaired locomotion activity, there is neither neuronal death nor gross anatomical abnormalities in motor circuit wiring (Briese et al., 2009). This suggests that functional deficits within the circuitry precede anatomical abnormalities and/or that the relevant anatomical defects have not been examined at high enough resolution. We lack quantitative data on the effect of loss of *smn* on worm locomotion over time.

To fill these gaps, we use non-invasive worm tracking and image processing techniques coupled with hydrodynamic models to extract quantitative kinematic (e.g. swimming speed) and dynamic (e.g. propulsive force) properties of *C. elegans* during swimming in a water-like buffer solution (M9, Brenner 1979). Previously, *smn-1(ok355)* null mutants have been shown to exhibit a dramatic and progressive decline in thrashing rate after L2 stage (Briese et al., 2009). With this in mind, we monitored each group's swimming gait at two different stages: L2 (early) and L2+3 days (late, Day 5) to examine if a reduction of *daf-2* signaling rescues locomotion deficit in *smn-1(ok355)*. We note that aged-matched control animals for smn-1 null animals at Day 5 develop to adults, while *smn-1(ok355)* or *smn-*

1(ok355);daf-2(e1370) arrest at L4 stage. Thus, L4 larva of wild type N2 and *daf-2(e1370)* are selected as control groups based on the most biomechanically-relevant developmental parameter: the nematode's body length. We note that the typical body lengths for early- and late-stage groups are 0.45 mm and 0.67 mm respectively.

6.1. Methods

Worms were transferred into 400 µl of M9 buffer contained in a sealed fluidic chamber 2 cm in diameter and 1 mm in depth. Image series of swimming nematodes were captured using a standard bright-field stereomicroscope and a CCD camera at 30 frames per second. We analyzed swimming images using in-house biomechanical profiling software. To eliminate boundary effects, we place the focal plane at the center of the chamber and out-of-focus recordings are discarded. Additionally, all individuals swim for a minimum four full undulatory cycles.

6.2. Results and discussion

Figure 24 summarizes the modification in swimming dynamics among a control group, the diseased group, and the rescue group. The left column shows the body shapes (nematode's centerlines) of three groups over one beating cycle, with red lines representing body shape during phases of the nematode's downstroke and blue lines representing body shape during the upstroke. From top to bottom, these groups are wild type N2, *smn-1(ok355)*, and *smn-1(ok355);daf-2(e1370)*. Using these body shapes, we can compute a number of properties to describe the swimming gait of each group including body curvature. Examples of this are shown in the right column, which displays kymographs of the worm's body curvature for one second of forward swimming (see methods section for more detail).

The striations of curvature clearly show beating patterns moving down the body of the nematode from head to tail; the slope of these stripes represent the wave speed, or the rate at which waves of curvature move down the body of the worm, and the rate at which the pat-

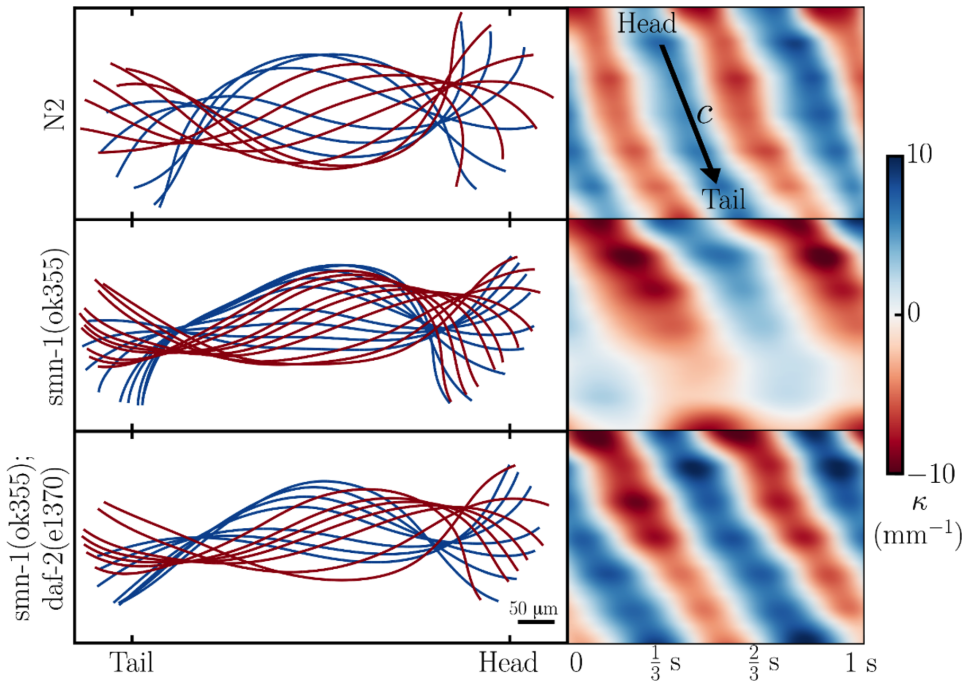

Figure 24: Body shapes over one full cycle and curvature kymographs for control group N2 (wildtype), a diseased group *smn-1(ok355)*, and a rescue group *smn-1(ok355);daf-2(e1370)*.

tern repeats itself represents the frequency of the worms beating. Curvature is again shown for three groups (from top to bottom: wild type N2, *smn-1(ok355)*, and *smn-1(ok355);daf-2(e1370)*). We observe, at least qualitatively, that the curvature patterns of *smn-1(ok355)* shows significant differences from that of healthy wild type N2 nematodes. Furthermore, it appears that the curvature pattern of *smn-1(ok355);daf-2(e1370)* seems similar to the wild type group, suggesting that a reduction in*daf-2* signaling may rescue the behavior of the *smn-1(ok355);daf-2(e1370)* group.

We further examine the data shown in Figure 24 using in-house biomechanical profiling algorithms by quantifying each group's swimming speed and beating frequency. At the L2 stage, the swimming speed of N2 is approximately 0.2 mm/s (Figure 25). There is no statistically significant difference among the swimming speeds of N2, *daf-2(e1370)*, *smn-1(ok355)*, and *smn-1(ok355);daf-2(e1370)* at the L2 stage ($p > 0.05$, Kruskal-Wallis test).

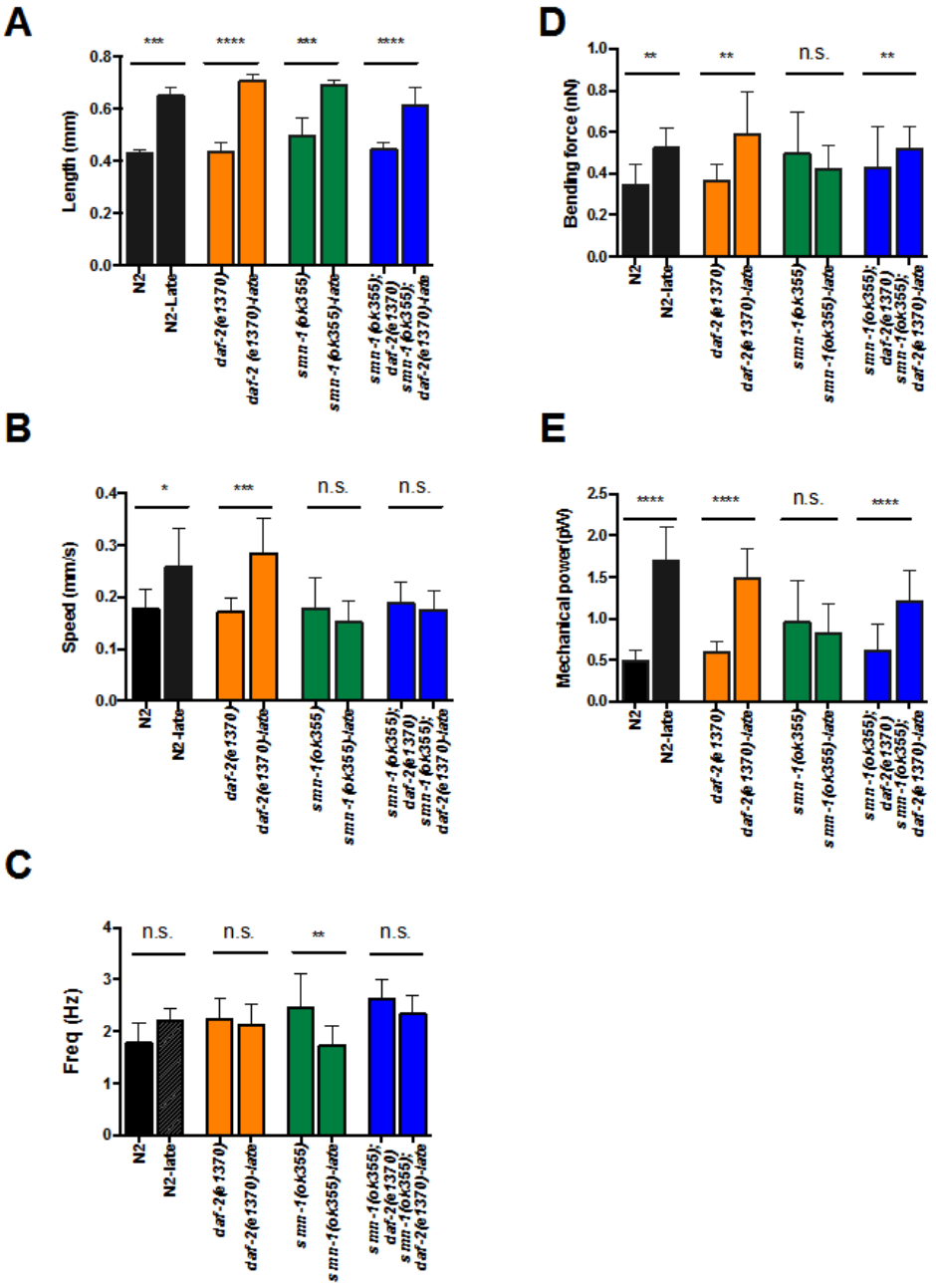

Figure 25: *(a)* Length, *(b)* swimming speed, *(c)* frequency, *(d)* bending force, and *(e)* mechanical power control groups N2 (wildtype) and the long-lived mutant *daf-2(e1370)*, a diseased group *smn-1(ok355)*, and a rescue group *smn-1(ok355);daf-2(e1370)*. Black bars represent standard error.

With developmental progression (late stage), wild type N2 and *daf-2(e1370)* significantly increase their swimming speed by 44% and 60%, respectively. In contrast, *smn-1(ok355)* and *smn-1(ok355);daf-2(e1370)* remain similar to their L2 stage swimming speeds even at Day 5, suggesting that the presence of *smn-1(ok355)* is impairing locomotion rate.

Next, we investigate the nematode's beating frequency. We observe the frequency of N2 remains statistically similar with developmental progression (1.8 Hz at the L2, and 2.2 Hz at the L4, $p > 0.05$, Kruskal-Wallis test) (Figure 25). For *smn-1(ok355)*, the beating frequency at the L2 stage is significantly higher than N2 (2.5 Hz vs. 1.8 Hz, $p < 0.05$, Kruskal-Wallis test) and decreases by 28% from the L2 stage to Day 5 of *smn-1(ok355)* from 2.5 Hz to 1.7 Hz ($p < 0.01$, Kruskal-Wallis test). We also find that the beating frequency of *smn-1(ok355);daf-2(e1370)* at the L2 stage is similar to the age-matched *smn-1(ok355)* (2.2 Hz vs. 2.5 Hz), but unlike the *smn-1(ok355)* group, *smn-1(ok355);daf-2(e1370)* is able to maintain its beating frequency through Day 5 in a fashion similar to wild type N2. This perhaps hints at an increase in coordination or signaling for *smn-1(ok355);daf-2(e1370)* compared to *smn-1(ok355)*.

While an analysis of these simple swimming kinematics reveals that the nematode's beating frequency appears to improve with the inactivation of *daf-2* signaling, the nematode's swimming speed appear to be unmodified. While swimming frequency and speed are important factors in describing the nematode's locomotion, there are of course other quantities that can be measured in order to elucidate the impact of *daf-2* including the swimming nematode's propulsive force and mechanical power. In their natural environments, C. elegans navigate diverse environments such as water and soil, generating propulsion via alternating contraction and relaxation of two dorsal and two ventral muscle groups along the length of the worm's body. Through the above observations of the worm's bending, we can use the hydrodynamic model Resistive Force Theory (RFT, (Gray and Hancock, 1955)) to estimate the propulsive force and mechanical power of C. elegans. We expect these two

measurements to provide much more detailed information about group differences, since they more directly probe muscle output and the energy expended via locomotion.

Typically, as a worm develops, we expect the propulsive force of the organism to increase; indeed, we find that both wildtype N2 and *daf-2(e1370)* controls exhibit an increase in propulsive force of 55% and 59%, respectively, when they grow from L2 to L4 stage ($p < 0.01$, Kruskal-Wallis test, Figure 25). In contrast, for *smn-1(ok355)*, the propulsive force remains the same (or slightly decreases) during the L2 to L4 developmental period, suggesting that muscle output is largely impaired. In contrast, *smn-1(ok355);daf-2(e1370)* shows an increase in bending force by 20% ($p < 0.01$, Kruskal-Wallis test) between the L2 and L4 states, suggesting that the decrease in *daf-2* signaling increases output of the dorsal and ventral muscles.

Furthermore, we measured the mechanical power of each group to estimate the rate of energy expenditure available for locomotion. We observe that wild type N2 and *daf-2(e1370)* significantly increase their mechanical power (250% and 150%, respectively) as they grow and develop (Figure 25). In stark contrast, *smn-1(ok355)* produces the same mechanical power at the L2 and Day 5 states, suggesting that during development, the worms are unable to increase their capacity for locomotion. At late stage (Day 5), the mechanical power of the *smn-1(ok355)* group is significantly lower than N2 (0.83 vs. 1.7, $p < 0.001$, Kruskal-Wallis test). Reduction of *daf-2* signaling (*smn-1(ok355);daf-2(e1370)*) significantly improves mechanical power compared to *smn-1(ok355)*, and the energy expenditure of *smn-1(ok355);daf-2(e1370)* is statistically indistinguishable from the late stage wild type group ($p > 0.05$, Kruskal-Wallis test)(Figure 25).

CHAPTER 7 : Summary and Future Work

7.1. Perform systematic studies of swimming in fluids with non-Newtonian viscosity behavior

We have investigated the effects of shear-thinning viscosity on the swimming kinematics and flow fields of the nematode *C. elegans* in solutions of a semi-rigid, rod-like polymer (XG) in buffer solution (M9). We find no significant differences between the observed kinematics in shear-thinning fluids and the kinematics in Newtonian fluids of similar viscosity, a result consistent with recent theoretical calculations (Vélez-Cordero and Lauga, 2013). Despite this experimental observation (unmodified kinematics), we find substantial differences between the resulting Newtonian and shear-thinning flow fields.

Temporal and spatial averages of velocity fields, along with a snapshot of the flow fields at one phase in the cycle, reveal a structural difference in the flow field near the head of the worm in shear-thinning fluids when compared to the Newtonian case. Streamlines reveal the major structural difference occurs within the dominant body vortex near the nematode's head; we quantify this effect by computing the circulation of the vortex, thereby accounting for strength and size. We find that an increase in shear-thinning behaviour leads to an enhancement in circulation, consistent with recent theoretical calculations (see Vélez-Cordero and Lauga (2013)). Furthermore, the shear-thinning flow fields reveal a decrease in average fluid velocity near the head of the organism and an increase near the tail. We find that the ratio of average fluid velocity at the tail to that at the head increases as the Carreau timescale λ_{Cr} increases, and that this effect plateaus once λ_{Cr} is similar to the timescale of the forward swimming motion, U/L.

Using each side of the energy balance for a low Reynolds number swimmer (Eq. 3.9), we find that *(i)* the mechanical power and *(ii)* the viscous dissipation rate suggest that the cost of swimming for an undulatory swimming in shear-thinning fluids is smaller than

the cost of swimming in a Newtonian fluid with the equivalent zero-shear viscosity. Furthermore, this cost of swimming is well-described by the scaling $P \sim \eta_{\text{eff}} U^2$ (Fig. 12*(b)*). Our experimental observations show good agreement with a recent theoretical scaling (Li and Ardekani, 2015) (Fig. 13). These results provide a framework for understanding of the cost of swimming in generalized Newtonian fluids, which can be predicted using only the fluid's rheology and simple swimming kinematics.

7.2. Examine swimming under anisotropic conditions, including confinement in non-Newtonian fluids

7.2.1. Swimming in anisotropic fluids

We have investigated the swimming behavior of the nematode *C. elegans* in semi-dilute and concentrated solutions of a rod-like polymer (XG). We find a rapid increase in the nematode's swimming speed as the polymer concentration increases (Fig 16*(c)*). This sudden increase in swimming speed occurs near the solution's transition from the semi-dilute to concentrated regime. We show that this increase in swimming speed is most likely related to the anisotropic response of the fluid microstructure to applied stress due to the nematode's swimming motion. In short, the undulatory swimming motion of *C. elegans* induces a structural anisotropy which leads to an increase in the *effective* drag coefficient ratio C_n/C_t and an enhancement in swimming speed U (Fig. 18*(c)*).

Experimentally measured velocity fields corroborate with the proposed mechanism. The PDFs of the velocities of tracer particles show important differences between semi-dilute and concentrated solutions (see Fig. 18*(a)* and *(b)*). While for the semi-dilute case both the tangential and normal velocity components collapse onto one another, we find a sharp difference between the two components at high velocities for nematodes swimming in concentrated solutions. In particular, we find that the tangential velocity distribution has a faster decay at high velocities than the normal direction, which indicates a relative en-

hancement in the normal component of momentum.

Our finding serves as a step towards understanding the locomotion of organisms in highly structured fluid environments such as human tissues, gels, and mucus. Such understanding can be important, for example, in modifying mucous systems to fend off bacterial infection, to treat human fertility disorders by altering the cervical fluid environment, and to better maintain ecological systems.

7.2.2. Swimming in confined viscoelastic fluids

We observe a steadily increasing swimming speed with decreasing channel width in the Newtonian case and and decreasing swimming speed and increasing transverse waving speed fA with decreasing channel width in viscoelastic cases. These phenomena appear to be caused by interaction between the nematode's flow field and the walls, which substantially modify the structure of the flow fields to produce a hyperbolic point with locally large fluid velocities and shear rates. This change in structure leads to a substantial increase in Wi near the body of the nematode, suggesting an increase in the viscoelastic stresses. The increase in viscoelastic stresses due to the presence of the walls suggests a mechanism for the observed inefficient swimming gait with decreasing channel width; despite *C. elegans* producing larger amplitude undulations and a larger typical transverse speed fA in viscoelastic fluids with decreasing channel width, the nematodes ultimately swim substantially slower, opposite of what the expected result in a Newtonian fluid. The combination of viscoelasticity and confinement serve to be a hindrance for nematodes and, by extension, other undulatory swimmers with similar motility gaits.

7.3. Apply swimming assays to the study of genetic disease

We find that an analysis of kinematic and dynamic biomechanical properties (i.e. frequency, propulsive force, and mechanical power) indicate that a reduction of daf-2 signaling has the potential to enhance the locomotion capability in smn-1(ok355). While these

statistically-significant modifications do not directly increase the swimming speed of the organism, they appear to rescue the beating patterns, muscle output, and the energy expenditure during swimming.

7.4. Future Work

A natural extension of this work is to consider the interaction of many swimming and non-Newtonian fluids. Examples including the study of collective motion in non-Newtonian fluids and the effects suspensions of active swimmers of the mechanical properties of shear-thinning and viscoelastic fluids. Systems of many swimmers may yield increasingly accurate models for biofilm formation in mucus, the mechanical properties and mixing of streams of organisms used in the production of biofuels, and the transport of organisms in ecological and biological flows.

BIBLIOGRAPHY

M. Alexander. *Introduction to soil microbiology*. R.E. Krieger, Malabar, FL, 1991.

M. Bees and O. Croze. Mathematics for streamlined biofuel production from unicellular algae. *Biofuels*, 5:53, 2014.

A. Benchabane and K. Bekkour. Rheological properties of carboxymethyl cellulose (cmc) solutions. *Colloid Polym. Sci.*, 286:1173–1180, 2008.

H. Berg and L. Turner. Movement of microorganisms in viscous environments. *Nature*, 278:349–351, 1979.

A. Bilbao, E. Wajnryb, S. Vanapalli, and J. Blawzdziewicz. Nematode locomotion in unconfined and confined fluids. *Phys. Fluids*, 25:081902, 2013.

S. Brenner. The genetics of *Caenorhabditis elegans*. *Genetics*, 77:71–94, 1974.

L. Byerly, R. Cassada, and R. Russell. The life cycle of the nematode *Caenorhabditis elegans*: I. wild-type growth and reproduction. *Dev. Biol.*, 51:23–33, 1976.

P. Carreau, D. DeKee, and R. Chhabra. *Rheology of polymeric systems*. Hanser, Munich, 1997.

J. Celli, B. Turner, N. Afdhal, S. Keates, I. Ghiran, C. Kelly, R. Ewoldt, G. McKinley, P. So, S. Erramilli, and R. Bansil. *Heliobacter pylori* moves through mucus by reducing mucin viscoelasticity. *Proc. Natl. Acad. Sci. USA*, 106:14321–14326, 2009.

S. Childress. *Mechanics of Swimming and Flying*. Cambridge University Press, 1981.

G. Colburn. *The anatomy of the fallopian tube*. Futura Publishing, 1986.

R. Cortez, L. Fauci, and A. Medovikov. The method of regularized stokeslets in three dimensions: Analysis, validation, and application to helical swimming. *Phys. Fluids*, 17: 1, 2005.

M. Dasgupta, B. Liu, H. Fu, M. Berhanu, K. Breuer, T. Powers, and A. Kudrolli. Speed of a swimming sheet in newtonian and viscoelastic fluids. *Phys. Rev. E*, 87:013015, 2013.

A. Dobrynin, R. Colby, and M. Rubenstein. Scaling theory of polyelectrolyte solutions. *Macromolecules*, 28:1859–1871, 1995.

M. Doi and S. Edwards. *The theory of polymer dynamics*. Oxford University Press, New York, 1988.

J. Du, J. Keener, R. Guy, and A. Fogelson. Low-Reynolds-number swimming in viscous two-phase fluids. *Phys. Rev. E*, 85:036304, 2012.

G. Elfring, E. Lauga, and S. (ed.) Spagnolie. *Complex Fluids in Biological Systems: Theory of Locomotion through Complex Fluids*. Springer, 2015.

L. Fauci and R. Dillon. Biofluidmechanics of reproduction. *Annu. Rev. Fluid Mech.*, 38: 371–394, 2006.

N. Francois, D. Lasne, Y. Amarouchene, B. Lounis, and H. Kellay. Drag enhancement with polymers. *Phys. Rev. Lett.*, 100:018302, 2008.

H. Fu, C. Wolgemuth, and T. Powers. Swimming speeds of filaments in nonlinearly viscoelastic fluids. *Phys. Fluids*, 21:033102–033110, 2009.

H. Fu, V. Shenoy, and T. Powers. Low-Reynolds-number swimming in gels. *EPL*, 91, 2010.

E. Gaffney, H. Gadelha, D. Smith, J. Blake, and J. Kirkman-Brown. Mammalian sperm motility: Observation and theory. *Annu. Rev. Fluid Mech.*, 43:501, 2011.

D. Gagnon and P. Arratia. The cost of swimming in generalized newtonian fluids: experiments with *C. elegans*. *J. Fluid Mech.*, 800:753–765, 2016.

D. Gagnon, X. Shen, and P. Arratia. Undulatory swimming in fluids with polymer networks. *Europhys. Lett.*, 104:14004, 2013.

D. Gagnon, N. Keim, and P. Arratia. Undulatory swimming in shear-thinning fluids: experiments with *Caenorhabditis elegans*. *J. Fluid Mech.*, 758:R3, 2014a.

D. Gagnon, N. Keim, X. Shen, and P. Arratia. Fluid-induced propulsion of rigid particles in wormlike micellar solutions. *Phys. Fluids*, 26:103101, 2014b.

J. Gray and G. Hancock. The propulsion of sea-urchin spermatozoa. *J. Exp. Biol.*, 32:802–814, 1955.

J. Gray and H. Lissmann. The locomotion of nematodes. *J. Exp. Biol.*, 41:135–154, 1964.

J. Guasto, K. Johnson, and J. Gollub. Oscillatory flows induced by microorganisms swimming in two dimensions. *Phys. Rev. Lett.*, 105:168102, 2010.

D. Guzick, J. Overstreet, P. Factor-Litvak, C. Brazil, S. Nakajima, C. Coutifaris, S. Carson, P. Cisneros, M. Steinkampf, J. Hill, D. Xu, and D. Vogel. Sperm morphology, motility, and concentration in fertile and infertile men. *New Engl. J. Med.*, 345:1388–1393, 2001.

G. Hancock. The self-propulsion of microscopic organisms through liquids. *Proc. R. Soc. Lon. Ser.-A*, 217:96–121, 1953.

M. Harman, S. Dunham-Ems, M. Caimano, A. Belperron, L. Bockenstedt, H. Fu, J. Radolf,

and C. Wolgemuth. The heterogenous motility of the Lyme disease spirochete in gelatin mimics dissemination through tissue. *Proc. Natl. Acad. Sci. USA*, 109:3059–3064, 2012.

L. Johnson, G. Welch, and W. Rens. The beltsville sperm sexing technology: high-speed sperm sorting gives improved sperm output for in vitro fertilization and ai. *J. Anim. Sci.*, 77:213, 1999.

C. Josenhans and S. Suerbaum. The role of motility as a virulence factor in bacteria. *Int. J. Med. Microbiol.*, 291:605–614, 2002.

G. Juarez, K. Lu, J. Sznitman, and P. E. Arratia. Motility of small nematodes in wet granular media. *Europhys. Lett.*, 92(4):44002, 2010.

S. Jung. *Caenorhabditis elegans* swimming in a saturated particulate system. *Phys. Fluids*, 22 (3):031903, 2010.

D. Katz and S. Berger. Flagellar propulsion of human sperm in cervical mucus. *Biorheology*, 17:169–175, 1980.

F. Katz. On the propulsion of micro-organisms near solid boundaries. *J. Fluid Mech.*, 64: 33–49, 2003.

J. Korta, D. Clark, and C. Gabel. Mechanosensation and mechanical load modulate the locomotory gait of swimming *C. elegans*. *J. of Exp. Biol.*, 210:2383–2389, 2007.

P. Krajacic, X. Shen, P. Purohit, P. Arratia, and T. Lamitina. Biomechanical profiling of *Caenorhabditis elegans* motility. *Genetics*, 191:1015–U1613, 2012.

R. Larson. *The structure and rheology of complex fluids*. Oxford University Press, New York, 1999.

E. Lauga. Propulsion in a viscoelastic fluid. *Phys. Fluids*, 19:083104–083113, 2007.

E. Lauga and R. Goldstein. Dance of the microswimmers. *Phys. Today*, 65:30–35, 2012.

E. Lauga and T. Powers. The hydrodynamics of swimming microorganisms. *Reports on Progress in Physics*, 72:096601, 2009.

K. Leptos, J. Guasto, J. Gollub, A. Pesci, and R. Goldstein. Dynamics of enhanced tracer diffusion in suspensions of swimming eukaryotic microorganisms. *Phys. Rev. Lett.*, 103, 2009.

A. Leshansky. Enhanced low-Reynolds-number propulsion in heterogeneous viscous environments. *Phys. Rev. E*, 80:051911, 2009.

G. Li and A. Ardekani. Hydrodynamic interaction of micro-swimmers near a wall. *Phys. Rev. E*, 90:013010, 2014.

G. Li and A. Ardekani. Undulatory swimming in non-newtonian fluids. *J. Fluid Mech.*, 784: R4, 2015.

J. Lighthill. Flagellar hydrodynamics. *SIAM Rev.*, 18:161–230, 1976.

T. Lim, J. Uhl, and R. Prudhomme. Rheology of self-associating concentrated xanthan solutions. *J. Rheol.*, 28:367–379, 1984.

B. Liu, T. Powers, and K. Breuer. Force-free swimming of a model helical flagellum in viscoelastic fluids. *Proc. Natl. Acad. Sci. USA*, 108:19516–19520, 2011.

Y. Magariyama and S. Kudo. A mathematical explaination of an increase in bacterial swimming speed with viscosity in linear-polymer solutions. *Biophys. J.*, 83:733–739, 2002.

T. Majumdar, E. Keaveny, and M. S. J. Zhang. Experiments and theory of undulatory locomotion in a simple structured medium. *J. R. Soc. Interface*, 9:1809–1823, 2012.

M.Backholm, R. Schulman, W. Ryu, and K. Dalnoki-Veress. Tangling of tethered swimmers: Interactions between two nematodes. *Phys. Rev. Lett.*, 113:5, 2014.

T. Montenegro-Johnson, A. Smith, D. Smith, D. Loghin, and J. Blake. Modelling the fluid mechanics of cilia and flagella in reproduction and development. *Eur. Phys. J. E*, 35:111, 2012.

T. Montenegro-Johnson, D. Smith, and D. Loghin. Physics of rheologically enhanced propulsion: Different strokes in generalized Stokes. *Phys. Fluids*, 25:081903, 2013.

T. Montenegro-Johnson, D. Gagnon, P. Arratia, and E. Lauga. Flow analysis of the low reynolds number swimmer *C. elegans*. *Phys. Rev. Fluids*, 1:053202, 2016.

T. D. Montenegro-Johnson, S. Michelin, and E. Lauga. A regularised singularity approach to phoretic problems. *Eur. Phys. J. E*, 38, 2015.

J. Münch, D. Alizadehrad, S. Babu, and H. Stark. Taylor line swimming in microchannels and cubic lattices of obstacles. *Soft Matter*, 12:7350–7363, 2016.

S. Nakamura, Y. Adachi, T. Goto, and Y. Magariyama. Improvement in motion efficiency of the sprirochete *Brachyspira pilosicoli* in viscous environments. *Biophys. J.*, 90:3019–3026, 2006.

V. Padmanabhan, Z. Khan, D. Solomon, A. Armstrong, K. Rumbaugh, S. Vanapalli, and J. Blawzdziewicz. Locomotion of *C. elegans*: A piecewise-harmonic curvature representation of nematode behavior. *PloS One*, 7:e40121, 2012.

J.-S. Park, D. Kim, J. Shin, and D. Weitz. Efficient nematode swimming in a shear thinning colloidal suspension. *Soft Matt.*, 12, 2016.

A. Patteson, A. Gopinath, M. Goulian, and P. Arratia. Running and tumbling with *E. coli* in polymeric solutions. *Sci. Rep.*, 5:15761, 2015.

T. Pedley, D. Brumley, and R. Goldstein. Squirmers with swirl: a model for *Volvox* swimming. *J. Fluid Mech.*, 798:165–186, 2016.

C. Pozrikidis. *Boundary integral and singularity methods for linearized viscous flow*. Cambridge Univ. Press, 1992.

C. Pozrikidis. *A practical guide to boundary element methods with the software library BEMLIB*. CRC Press, 2002.

E. Purcell. Life at low Reynolds number. *Am. J. Phys.*, 45(1):3–11, 1977.

B. Qin, A. Gopinath, J. Yang, J. Gollub, and P. Arratia. Flagellar kinematics and swimming of algal cells in viscoelastic fluids. *Sci. Rep.*, 5:9190, 2015.

F. Qiu and B. Nelson. Magnetic helical micro- and nanorobots: Toward their biomedical applications. *Engineering*, 1:21, 2015.

A. Rodd, D. Dunstan, and D. Boger. Characterisation of xanthan gum solutions using dynamic light scattering and rheology. *Carbohyd. Polym.*, 45:159–174, 2000.

D. Saintillan and M. Shelley. Emergence of coherent structures and large-scale flows in motile suspensions. *J. R. Soc. Interface*, 9:571–585, 2012.

W. Schneider and R. Doetsch. Effect of viscosity on bacterial motility. *J. Bacteriol.*, 117: 696–701, 1974.

R. Schulman, M. Backholm, W. Ryu, and K. Dalnoki-Veress. Undulatory microswimming near solid boundaries. *Phys. Fluids*, 26:101902, 2014.

X. Shen and P. Arratia. Undulatory swimming in viscoelastic fluids. *Phys. Rev. Lett.*, 106: 208101, 2011.

D. Smith. A boundary element regularized stokeslet method applied to cilia- and flagella-driven flow. *Proc. R. Soc. Lond. A*, 465:3605, 2009.

K. Song, Y. Kim, and G. Chang. Rheology of concentrated xanthan gum solutions: Steady shear flow behavior. *Fiber Polym.*, 7:129–138, 2006.

S. Spagnolie, editor. *Complex Fluids in Biological Systems*. Springer, 2015.

J. Sznitman, P. Purohit, P. Krajacic, T. Lamitina, and P. Arratia. Material properties of *Caenorhabditis elegans* swimming at low Reynolds number. *Biophys. J.*, 98:617–626, 2010a.

J. Sznitman, X. Shen, R. Sznitman, and P. Arratia. Propulsive force measurements and flow behavior of undulatory swimmers at low Reynolds number. *Phys. Fluids*, 22:121901, 2010b.

R. Sznitman, M. Gupta, G. Hager, P. Arratia, and J. Sznitman. Multi-environment model estimation for motility analysis of *Caenorhabditis elegans*. *PLoS ONE*, 5:e11631, 2010c.

G. Taylor. Analysis of the swimming of microscopic organisms. *Proc. R. Soc. Lon. Ser.-A*, 209(1099):447–461, 1951.

J. Teran, L. Fauci, and M. Shelley. Viscoelastic fluid response can increase the speed and efficiency of a free swimmer. *Phys. Rev. Lett.*, 104:038101, 2010.

B. Thomases and R. Guy. Mechanisms of elastic enhancement and hindrance for finite-length undulatory swimmers in viscoelastic fluids. *Phys. Rev. Lett.*, 113:098102, 2014a.

B. Thomases and R. Guy. Mechanisms of elastic enhancement and hindrance for finite-length undulatory swimmers in viscoelastic fluids. *Phys. Rev. Lett.*, 113:098102, 2014b.

M. Tracy and R. Pecora. Dynamics of rigid and semirigid rodlike polymers. *Ann. Rev. of Phys. Chem.*, 43:525–557, 1992.

J. Vélez-Cordero and E. Lauga. Waving transport and propulsion in a generalized Newtonian fluid. *J. Non-Newton. Fluid.*, 199:37–50, 2013.

J. White, E. Southgate, J. Thomson, and S. Brenner. The structure of the nervous system of the nematode *Caenorhabditis elegans*. *Phil. Trans. R. Soc. B*, 314:1–340, 1986.

N. Wyatt and M. Liberatore. Rheology and viscosity scaling of the polyelectrolyte xanthan gum. *J. Appl. Polym. Sci.*, 114:4076–4084, 2009.

S. Yazdi, A. Ardekani, and A. Borhan. Locomotion of microorganisms near a no-slip boundary in a viscoelastic fluid. *Phys. Rev. E*, 90:043002, 2014.

S. Yazdi, A. Ardekani, and A. Borhan. Swimming dynamics near a wall in a weakly elastic fluid. *J. Nonlinear Sci.*, 25:1153–1167, 2015.

J. Yuan, D. Raizen, and H. Bau. High-throughput, motility-based sorter for microswimmers such as *C. elegans*. *Proc. Natl. Acad. Sci.*, 112:3606, 2015.

M. Zirnsak, D. Boger, and V. Tirtaatmadja. Steady shear and dynamic rheological properties of xanthan gum solutions in viscous solvents. *J. Rheol.*, 43:627–650, 1999.